

The MUSE 3D view of feedback in a high-metallicity radio galaxy at $z = 2.9$

M. Silva,^{1,2★} A. Humphrey,^{1★} P. Lagos,¹ M. Villar-Martín,³ S. G. Morais,^{1,2}
S. di Serego Alighieri,⁴ A. Cimatti,⁵ R. Fosbury,⁶ R. A. Overzier,⁷
J. Vernet⁸ and L. Binette⁹

¹*Institute of Astrophysics and Space Sciences, Universidade do Porto, CAUP, Rua das Estrelas, P-4150-762 Porto, Portugal*

²*Departamento de Física e Astronomia, Faculdade de Ciências, Universidade do Porto, R. Campo Alegre 687, P-4169-007 Porto, Portugal*

³*Departamento de Astrofísica, Centro de Astrobiología, Ctra de Torrejón a Ajalvir km 4, E-28850, Madrid, Spain*

⁴*INAF - Osservatorio Astrofisico di Arcetri, Largo E. Fermi 5, I-50125 Firenze, Italy*

⁵*Dipartimento di Astronomia, Università di Bologna, Via Ranzani 1, I-40127 Bologna, Italy*

⁶*European Southern Observatory, Karl Schwarzschild Str 2, D-85748 Garching, Germany*

⁷*Observatório Nacional, Rua José Cristino 77, São Cristóvão, Rio de Janeiro-RJ, 20921-400, Brazil*

⁸*European Southern Observatory, Karl-Schwarzschild-Str 2, D-85748 Garching, Germany*

⁹*Instituto de Astronomía, Universidad Nacional Autónoma de México, Ap. 70-264, 04510 México D.F., México*

Accepted 2017 November 15. Received 2017 November 15; in original form 2017 July 29

ABSTRACT

We present a detailed study of the kinematic, chemical and excitation properties of the giant Ly α emitting nebula and the giant H I absorber associated with the $z = 2.92$ radio galaxy MRC 0943–242, using spectroscopic observations from Very Large Telescope (VLT)/Multi Unit Spectroscopic Explorer (MUSE), VLT/X-SHOOTER and other instruments. Together, these data provide a wide range of rest-frame wavelength (765–6378 Å at $z = 2.92$) and 2D spatial information. We find clear evidence for jet gas interactions affecting the kinematic properties of the nebula, with evidence for both outflows and inflows being induced by radio-mode feedback. We suggest that the regions of relatively lower ionization level, spatially correlated with the radio hotspots, may be due to localized compression of photoionized gas by the expanding radio source, thereby lowering the ionization parameter, or due to a contribution from shock-heating. We find that photoionization of supersolar metallicity gas ($Z/Z_{\odot} = 2.1$) by an active galactic nuclei-like continuum ($\alpha = -1.0$) at a moderate ionization parameter ($U = 0.018$) gives the best overall fit to the complete X-SHOOTER emission-line spectrum. We identify a strong degeneracy between column density and Doppler parameter such that it is possible to obtain a reasonable fit to the H I absorption feature across the range $\log N(\text{H I}/\text{cm}^{-2}) = 15.20$ and 19.63, with the two best fitting occurring near the extreme ends of this range. The extended H I absorber is blueshifted relative to the emission-line gas, but shows a systematic decrease in blueshift towards larger radii, consistent with a large-scale expanding shell.

Key words: galaxies: active – galaxies: evolution – galaxies: high-redshift – galaxies: individual: MRC 0943–242 – galaxies: ISM – quasars: absorption lines – quasars: emission lines.

1 INTRODUCTION

The study of high-redshift galaxies ($z \gtrsim 2$) allows us to look back to the young Universe, giving us the opportunity to witness and understand the processes by which galaxies form and evolve. In particular, powerful active galaxies such as high- z radio galaxies (HzRGs) or quasars offer the chance to examine a crucial phase in the evolution of massive galaxies, when the host galaxy is still

relatively gas rich and when radio- and quasar-mode feedback is also taking place. As such, HzRGs represent laboratories for studying the interplay between the ‘ingredients’ of galaxy formation, such as active galactic nuclei (AGN), gas, stars, feedback and other processes.

Many powerful HzRGs (or quasars) lie within giant haloes¹ of gas that are prodigious sources of Ly α (and other emission lines), and

* E-mail: marckelson@gmail.com (MS); andrew.humphrey.mexico@gmail.com (AH)

¹ These haloes are sometimes also known as the ‘extended emission-line region’, the ‘extended narrow-line region’ or ‘Ly α blobs’.

which have sizes often exceeding 100 kpc (Fosbury et al. 1982; di Serego Alighieri 1988; McCarthy et al. 1990; van Ojik et al. 1997; Pentericci et al. 1998; Francis et al. 2001; Reuland et al. 2003; Humphrey et al. 2013a; Cantalupo et al. 2014; Swinbank et al. 2015; Borisova et al. 2016; Cai et al. 2017).

These haloes have typical masses in gas of $\sim 10^{9-10} M_{\odot}$, Ly α luminosities up to $\sim 10^{45}$ erg s $^{-1}$ and estimated electron densities of a few to several hundred cm $^{-3}$ (McCarthy 1993; Reuland et al. 2003; Villar-Martín et al. 2003; Sánchez & Humphrey 2009; Humphrey et al. 2013a; Cantalupo et al. 2014; Cai et al. 2017). Typically the haloes can be divided into two kinematic and structural components: a high surface brightness region showing a clumpy, irregular morphology (Reuland et al. 2003) often aligned with the radio jets (McCarthy, Spinrad & van Breugel 1995) and characterized by extreme kinematics (full width at half-maximum (FWHM) > 1000 km s $^{-1}$; van Ojik et al. 1997; Villar-Martín et al. 2003; Humphrey et al. 2006), and a low surface brightness region sometimes extending beyond the maximum extent of the radio structures, showing relatively quiescent kinematics (FWHM $\lesssim 1000$ km s $^{-1}$) and no clear relationship with the radio source (van Ojik et al. 1996, 1997; Villar-Martín et al. 2002; Sánchez & Humphrey 2009). In addition, Humphrey et al. (2007) proposed that the quiescent gas of some HzRGs are in infall towards the central regions of the host galaxy, though it is not clear whether the infalling gas has an external origin, or is instead a back-flow of material after the passage of a large-scale outflow.

The ionization of the Ly α haloes of HzRGs is not fully understood, but several different mechanisms have been proposed, including photoionization by the central AGN (see McCarthy et al. 1990; Villar-Martín et al. 2003; Geach et al. 2009; Kollmeier et al. 2010; Cai et al. 2017), cooling radiation (see Haiman, Spaans & Quataert 2000; Steidel et al. 2000; Fardal et al. 2001; Dijkstra, Haiman & Spaans 2006; Yang et al. 2006; Faucher-Giguère et al. 2010; Rosdahl & Blaizot 2012), shocks driven by radio jets (see Emonts et al. 2005; Villar-Martín et al. 2007; Humphrey et al. 2008b) or resonant scattering (for Ly α) (see Gould & Weinberg 1996; Dijkstra et al. 2006; Villar-Martín et al. 2007; Dijkstra & Loeb 2009; Humphrey et al. 2013b; Cantalupo et al. 2014; Yang et al. 2014).

Other structures that are also not fully understood are the extended Ly α absorbers that are associated with roughly half of all radio galaxies at $z > 2$ (van Ojik et al. 1997; Jarvis et al. 2003; Wilman et al. 2004). They are at least as spatially extended as the Ly α haloes and appear to have column densities in the range $\sim 10^{14-20}$ cm $^{-2}$ (Röttgering et al. 1995; van Ojik et al. 1997; Binette et al. 2000; Jarvis et al. 2003; Wilman et al. 2004; Binette et al. 2007), with properties suggestive of an expanding shell with covering factor of, or approaching, unity (see Binette et al. 2000; Jarvis et al. 2003; Wilman et al. 2004; Binette et al. 2007). It has been suggested that these giant absorbing structures are the product of a past feedback event in the galaxy (e.g. Binette et al. 2006), and that their properties are somehow related to the size or passage of the radio jets (van Ojik et al. 1997). The presence of this type of shell around some HzRGs may have important implications for the escape of Ly α and ionizing photons.

In this paper, we present previously unpublished VLT X-SHOOTER² spectroscopy of the $z = 2.92$ HzRG MRC 0943–242, and pool this data with archival spectroscopic data from other VLT

instruments [Multi Unit Spectroscopic Explorer (MUSE) and Ultraviolet and Visual Echelle Spectrograph], spectra from the Anglo-Australian Telescope and Keck II, in order to conduct a detailed study of the spatially resolved kinematics and ionization of this galaxy’s large-scale Ly α emitting halo and its large-scale H I absorber. Gullberg et al. (2016) presented a primarily morphological study of this object combining the MUSE data set with multiwavelength data (see Section 2 below); here, we present a detailed study of the kinematic and ionization properties of the Ly α halo and the large-scale Ly α absorbing structure.

The paper is organized as follows. In Section 2, we describe the key previous results from the literature concerning this well-studied HzRG. In Section 3, we introduce the selected observations and data reduction for MRC 0943–242. In Section 4, we discuss our observational results. In Section 5, we discuss the physical properties and several powering mechanisms that could be responsible for such extended Ly α emission and Ly α absorber. In Section 6, we give a brief summary concluding our results. A $\Omega_{\Lambda} = 0.713$, $\Omega_{\text{m}} = 0.287$ and $H_{\odot} = 69.3$ km s $^{-1}$ Mpc $^{-1}$ (Hinshaw et al. 2013) cosmology is adopted in this paper so that 1 arcsec corresponds to 7.94 kpc at the redshift of our target ($z = 2.92$).

2 MRC 0943–242: PREVIOUS RESULTS

MRC 0943–242 was first catalogued in the Molonglo Reference Catalogue (Large et al. 1981), and selected as a possible HzRG on the basis of its ultrasteep radio spectrum by Röttgering et al. (1994). Optical imaging and spectroscopy confirmed the high redshift of this galaxy ($z = 2.92$; Röttgering et al. 1995).

The radio continuum of MRC 0943–242 has a simple double-morphology (Fanaroff–Riley Class II), consisting of two bright hotspots separated by 3.9 arcsec, with no core detected, at 1.4, 4.7 and 8.2 GHz (Röttgering et al. 1995; Carilli et al. 1997). Its spectral index between 1.5 and 30 GHz is $\alpha = -1.44$ (Emonts et al. 2011). With a 1.4 GHz radio power of $10^{35.4}$ erg s $^{-1}$ Hz $^{-1}$ (De Breuck et al. 2000), this is among the most radio-luminous galaxies known.

Rest-frame ultraviolet and optical *Hubble Space Telescope* (HST) images of MRC 0943–242 show a bright, elongated and curved morphology, with a close alignment between the major axis of this emission and that of the radio source (Pentericci et al. 1999, 2001). Using Keck II spectropolarimetry, Vernet et al. (2001) found the extended UV continuum emission along the radio/optical axis to be significantly polarized ($P_{\%} = 6.6 \pm 0.9$ per cent at ~ 1250 – 1400 Å) with the electric field vector approximately perpendicular to this axis, indicating a substantial contribution from scattered AGN continuum (22–66 per cent), but still allowing a potentially significant contribution from young stars (14–53 per cent). Along the radio/optical axis, Vernet et al. (2001) also estimated that nebular continuum emission contributes around 20 per cent of the UV continuum. Ground-based *K*-band imaging shows a rounded and more centrally concentrated morphology than seen in the optical images (van Breugel et al. 1998). Moreover, studying the contribution of the host galaxy stellar emission at rest-frame *H* band, Seymour et al. (2007) estimated the stellar luminosity of the radio galaxy that implied stellar mass of $\log(M_{\star}/M_{\odot}) = 11.22^{+0.15}_{-0.07}$. This HzRG also appears to be located in a proto-cluster (Venemans et al. 2007).

Spectroscopic studies have revealed that MRC 0943–242 is embedded within a giant Ly α halo (Röttgering et al. 1995, 1997; Binette et al. 2000; Jarvis et al. 2003; Villar-Martín et al. 2003; Venemans et al. 2007; Gullberg et al. 2016). Using Keck II

² We abbreviate X-SHOOTER to ‘XSH’ in some tables and figures in the interest of brevity.

Table 1. Long-slit and IFU spectroscopic observations. Column (1): instruments used in the observation; column (2): period during which the observation was made; column (3): spectral resolution of the instrument; column (4): aperture of the spectrum extraction; column (5): slit width; column (6): total observation time; column (7): spatial sampling; and column (8): position angle.

Instrument	Date	Resolution (km s^{-1})	Aperture (arcsec)	Slit width (arcsec)	Exp. time (s)	Scale/pixel (arcsec)	PA ($^{\circ}$)
(1)	(2)	(3)	(4)	(5)	(6)	(7)	(8)
XSH SLIT	2009 March	39, 32, 51	0.75, 0.8	1.0, 0.9	9000	0.16, 0.21	55
XSH IFU	2009 March	29, 22, 39	0.8	–	1700	0.16, 0.21	55
MUSE IFU	2014 February	100	0.8	–	3600	0.20	45,135,225
UVES	2001 December	7	1.0	1.2	10 800	0.18	74
AAT	1993 April, 1995 March	91	0.79	1.6	25 000	0.79	74
LRIS	1997 December	493	0.856	1.0	13 800	0.214	73

spectroscopy, Villar-Martín et al. (2003) found that the Ly α halo is metal enriched and has a high surface brightness, kinematically perturbed region ($\text{FWHM} \gtrsim 1000 \text{ km s}^{-1}$) within the spatial extent of the radio structure, and a giant low surface brightness region with quieter kinematics ($\text{FWHM} \lesssim 600 \text{ km s}^{-1}$) surrounding the entire object. Villar-Martín et al. (2003) and Humphrey et al. (2006) argued that the close spatial association between the kinematically perturbed gas and the radio structures suggests that jet–gas interactions are responsible for the kinematic perturbation in the high surface brightness regions. Furthermore, Humphrey et al. (2006) found that the kinematically more perturbed gas has a lower level of ionization than the quiescent gas, possibly due to the impact of shocks on the former.

Röttgering et al. (1995) detected a strong and spatially extended absorption feature in the profile of the Ly α line. By fitting the Ly α velocity profile, Röttgering et al. (1995), Binette et al. (2000), Jarvis et al. (2003) and Gullberg et al. (2016) have estimated the H I column density of the absorbing gas to be $\log N(\text{H I}/\text{cm}^{-2}) \sim 19$. It has been suggested that this absorbing structure is a large-scale shell that might surround the radio galaxy and its Ly α halo (Binette et al. 2007; Gullberg et al. 2016). Gas mass estimates for this absorbing structure range from $\gtrsim 10^9 M_{\odot}$ to $10^{12} M_{\odot}$ (see Binette et al. 2007; Gullberg et al. 2016).

In addition, Binette et al. (2000) detected the C IV doublet in absorption, with a column density $\log N(\text{C IV}/\text{cm}^{-2}) = 14.5 \pm 0.1$ and a redshift close to that of the main Ly α absorber. Based on the ratio of column densities derived from the Ly α and C IV absorption features, Binette et al. (2000) argued that the absorbing structure has a low metallicity ($Z = 0.01Z_{\odot}$) and is not co-spatial with the ionized gas responsible for the detected emission lines; the authors suggest that the absorbing gas represents material expelled from the HzRG during an earlier phase of starburst activity (see Binette et al. 2006, 2007).

Gullberg et al. (2016) presented a study of MRC 0943–242, combining ALMA sub-millimetre observations and MUSE Integral Field Unit (IFU) spectroscopy to perform a multiwavelength morphological study of the AGN, starburst and molecular gas components of the galaxy. They report a highly complex morphology, with a reservoir of molecular gas offset by $\sim 90 \text{ kpc}$ from the AGN, and identify a linear feature that emits Ly α , CO lines and dust continuum that they suggest may be due to an accretion flow on to the radio galaxy. Assuming that the main extended absorber surrounds the HzRG and has a roughly spherical shape, Gullberg et al. (2016) estimated a total gas mass of the main Ly α absorber of $M(\text{H I}) \gtrsim 3.8 \times 10^9 M_{\odot}$.

In summary, the observational properties of MRC 0943–242 make it an excellent target for a detailed case study into various processes that are expected to play an important role in the evo-

lution of massive galaxies, particularly the interplay between the ‘ingredients’ of galaxy formation, such as AGN, gas, stars, feedback, and gas accretion.

3 OBSERVATIONS

This study makes use of deep spectroscopic observations (proprietary and archival) from several different telescopes and instruments (see Table 1).

3.1 X-SHOOTER long-slit and IFU spectra

Here, we present previously unpublished X-SHOOTER (see Vernet et al. 2011) intermediate-resolution échelle spectroscopic observations of MRC 0943–242, obtained at the VLT UT3 on 2009 March 18 and May 3–5, during commissioning of the instrument under the programme 60.A-9022(C). The wavelength range of X-SHOOTER (3000–25 000 Å) provides a continuous rest-frame wavelength range of 765–6378 Å at $z = 2.92$, within which are expected to lie a multitude of diagnostically important emission or absorption lines. The pixel scale is $\sim 0.15 \text{ arcsec}$ for ultraviolet - blue (UVB) and visible (VIS) arms, and $\sim 0.20 \text{ arcsec}$ for the near-infrared (NIR) arm.

The X-SHOOTER observations were taken in two different modes: long-slit and IFU. In long-slit mode, the slit widths were 1.0 arcsec (UVB), 0.9 arcsec (VIS) and 0.9 arcsec (NIR). In IFU mode, the $4 \text{ arcsec} \times 1.8 \text{ arcsec}$ field of view was reformatted into $12 \text{ arcsec} \times 0.6 \text{ arcsec}$ pseudo-slits.

The integration time using the slit mode was split into $6 \times 1500 \text{ s}$ exposures for the UVB and VIS arms, and $6 \times 500 \text{ s}$ exposures for the NIR arm, with the slit oriented at a position angle (PA) of 55° . The slit observations were made in nodding mode. In IFU mode, the integration time was split into $1 \times 1700 \text{ s}$ for UVB arm, $1 \times 1700 \text{ s}$ for VIS arm and $3 \times 600 \text{ s}$ for NIR arm, with the PA identical to that used for the slit observations. The IFU observations were made in offset mode.

The data were processed using European Southern Observatory’s X-SHOOTER reduction pipeline, which performs bias/dark subtraction, background subtraction, flat-fielding, order tracing and merging, wavelength calibration, and finally flux calibration, for which the spectrophotometric standard star EG274 was used. The spectral resolution (FWHM) measured from the sky-lines was $\sim 39 \text{ km s}^{-1}$ (UVB), $\sim 32 \text{ km s}^{-1}$ (VIS) and $\sim 51 \text{ km s}^{-1}$ (NIR) on slit mode, and $\sim 29 \text{ km s}^{-1}$ (UVB), $\sim 22 \text{ km s}^{-1}$ (VIS) and $\sim 39 \text{ km s}^{-1}$ (NIR) on IFU mode.

The data were corrected for Galactic extinction using the NOAO IRAF task DEREDDEN, assuming $E(B - V) = 0.0512$ ($A_V = 0.1587$)

and the empirical selective extinction function of Cardelli, Clayton & Mathis (1989).

3.2 VLT MUSE IFU spectrum

We also make use of IFU spectroscopy that was obtained using the MUSE (Bacon et al. 2010) at the VLT UT4 on 2014 February 21, during the first commissioning run of the instrument (see Bacon et al. 2014) under the program 60.A-9100(A). Wide Field Mode was used, resulting in a field of view of $1\text{ arcmin} \times 1\text{ arcmin}$ at 0.2 arcsec spatial sampling. The wavelength range is $4650\text{--}9300\text{ \AA}$ and the mean spectral resolution is $\sim 100\text{ km s}^{-1}$ (FWHM). The target was observed for a total of 3600 s, which was split into $3 \times 1200\text{ s}$ exposures oriented at the PAs 45° , 135° and 225° . Full details of the MUSE observations, their reduction and some analysis have been previously published by Gullberg et al. (2016).

3.3 Keck II LRIS long-slit spectrum

Additional spectral information comes from a Low-Resolution Imaging Spectrometer (hereafter LRIS) spectrum taken at the Keck II 10-m telescope on 1997 December 27 (see Vernet et al. 2001) under the program C56L. The observation was done in polarization mode with the spectrum covering a wavelength range of $\sim 3900\text{--}9000\text{ \AA}$, and a spectral resolution of $\sim 493\text{ km s}^{-1}$ (FWHM). The 1 arcsec slit was oriented at a PA of 73° , i.e. along the radio axis. This spectrum has been presented and discussed in several previous publications (Vernet et al. 2001; Villar-Martín et al. 2002, 2003; Humphrey et al. 2006, 2007). See Vernet et al. (2001) for full details of the observation and reduction of these data.

3.4 VLT UVES archival spectrum

To complement the above observations, we have also made use of VLT Ultraviolet and Visual Echelle Spectrograph (hereafter UVES) observations on the night of 2001 December 8–9 of the radio galaxy, previously published by Jarvis et al. (2003). The spectrum comprises only the red arm and is centred on 5200 \AA so as to include Ly α and C IV, and the spectral resolution is $\sim 7\text{ km s}^{-1}$ (FWHM). The raw spectra taken under the program 68.B-0086(A) were obtained from the ESO VLT/UVES archive and were reduced using the UVES pipeline in which the data were automatically bias subtracted, flat-fielded, wavelength calibrated using Th–Ar arc lamp spectra, and flux calibrated using the spectrophotometric standard star LTT3864. The spectrum was corrected for Galactic extinction with IRAF’s DEREDDEN task, using $E(B - V) = 0.0512$ and the extinction function of Cardelli et al. (1989).

3.5 AAT RGO archival spectrum

In addition, a spectrum of MRC 0943–242 taken using the RGO spectrograph of the Anglo Australian Telescope (hereafter AAT) is used, which was previously published by Röttgering et al. (1995) and Binette et al. (2000). The spectrum covers the spectral regions around Ly α , C IV and He II at a resolution of $\sim 91\text{ km s}^{-1}$ (FWHM) with a slit PA of 74° , i.e. aligned with the radio axis. The raw spectra were obtained from the AAT archive and were bias subtracted, flat-fielded and then wavelength calibrated using Cu–Ar arc lamp spectra. In addition, flux calibration was done with the spectrophotometric standard stars FEIGE110 and LTT3864. Finally, the

spectrum was corrected for Galactic extinction using IRAF’s DEREDDEN, assuming $E(B - V) = 0.0512$ ($A_V = 0.1587$) and the extinction curve of Cardelli et al. (1989).

4 DATA ANALYSIS

4.1 Emission and absorption line fitting

4.1.1 Fitting routine

We created a PYTHON routine to fit the emission and absorption line parameters, with Gaussian and Voigt profiles being used to model the emission and absorption lines, respectively. The routine minimizes the sum of the squares of the difference between the model and data using the LMFIT algorithm (Newville et al. 2014). Parameters for the best fits are shown in Tables 2, 3, 4, and also Tables A1, A2 and A3.

4.1.2 Ly α and the degeneracy in N and b

The Ly α profile was parametrized assuming that the underlying emission line is a single Gaussian, and adopting Voigt profiles for the superimposed H I absorption features. Fig. 1 shows the 1D spectra of the Ly α emission line from the X-SHOOTER observations of MRC 0943–242. In addition, Fig. A1 shows the Ly α profile from the other telescopes/instruments.

When fitting absorption lines there can be a strong degeneracy between column density (N) and the Doppler width (b), and we find this to be the case with the main H I absorption feature seen in the Ly α profile of MRC 0943–242. We find two widely separated ‘best fitting’ to the column density of this absorber, one at $\log N(\text{H I}/\text{cm}^{-2}) = 15.20$ with $b \sim 153\text{ km s}^{-1}$ ($\tilde{\chi}_v^2 = 0.08$), and another at $\log N(\text{H I}/\text{cm}^{-2}) = 19.63$ with $b \sim 52\text{ km s}^{-1}$ ($\tilde{\chi}_v^2 = 0.07$).

We illustrate this degeneracy in Fig. 2, where we show column density ($N(\text{H I})$) versus reduced chi-square ($\tilde{\chi}_v^2$). With the exception of the two ‘best fitting’, the data points in this figure were obtained by running our fitting code with $N(\text{H I})$ fixed at specific values, but with all other parameters left free to vary. In addition to the presence of the two ‘best fitting’, Fig. 2 also illustrates the presence of a broad range of intermediate $N(\text{H I})$ values where the fits are still reasonably good.

Throughout this paper, we will ensure that the degeneracy described above is fully taken into account when we derive properties of the extended H I absorber. Where we make use of the flux of the Ly α emission line (e.g. Section 5.2), we adopt the absorption-corrected flux obtained from our $\log N(\text{H I}/\text{cm}^{-2}) = 19.63$ fit to the line profile ($20.27 \pm 0.38 \times 10^{-16}\text{ erg cm}^{-2}\text{ s}^{-1}$). Using instead the flux obtained from our $\log N(\text{H I}/\text{cm}^{-2}) = 15.20$ fit ($17.64 \pm 0.38 \times 10^{-16}\text{ erg cm}^{-2}\text{ s}^{-1}$) does not have any significant impact on our conclusions.

4.1.3 C IV

The methodology used to fit the C IV profile is similar to that used for Ly α . Because C IV is a doublet, two Gaussians were used for the emission and two Voigt profiles for the absorption, with the doublet’s (rest-frame) wavelength separation set to its theoretical value (see Figs 3 and A2). In the case of the emission components, we set the flux ratio $C\text{ IV } \lambda 1548.2/C\text{ IV } \lambda 1550.8$ to 0.5 and constrained both lines to have equal FWHM and redshift (z). For the absorption lines, we constrained both lines to have the same values for z , b and N .

Table 2. Measurements of the rest-frame UV and optical emission lines obtained with the fitting routine. Ly α_{15} and Ly α_{19} correspond to the lower ($\log N(\text{H I}/\text{cm}^{-2}) \sim 15.20$) and higher ($\log N(\text{H I}/\text{cm}^{-2}) \sim 19.63$) column density results, respectively. See Table A1 for other telescopes/instruments.

Line	λ_{rest} Å	λ_{obs} Å	Line flux ($\times 10^{-16}$ erg cm^{-2} s^{-1})	FWHM (km s^{-1})	Δv (km s^{-1})
X-SHOOTER SLIT					
O VI+C II	1031.9, 1037.6	$4050.0 \pm 0.7, 4072.4 \pm 0.7$	1.57 ± 0.24	869 ± 100	6 ± 48
Ly α_{15}	1215.7	4769.8 ± 0.1	17.64 ± 0.29	1557 ± 18	-84 ± 6
Ly α_{19}	1215.7	4769.1 ± 0.1	20.27 ± 0.38	1458 ± 16	-126 ± 5
N V	1238.8, 1242.8	$4858.7 \pm 1.0, 4874.3 \pm 1.0$	0.62 ± 0.11	883 ± 130	-204 ± 64
C IV	1548.2, 1550.8	$6076.2 \pm 0.5, 6086.4 \pm 0.3$	3.02 ± 0.20	1045 ± 53	-1 ± 23
He II	1640.4	6436.5 ± 0.26	2.05 ± 0.08	1018 ± 32	0 ± 12
C III]	1906.7, 1908.7	$7481.9 \pm 0.6, 7489.9 \pm 0.6$	1.11 ± 0.07	1087 ± 59	-49 ± 22
C II]	2325.4, 2326.9	$9123.2 \pm 2.0, 9129.2 \pm 2.0$	0.55 ± 0.09	1298 ± 181	-105 ± 64
[Ne IV]	2421.8, 2424.4	$9502.6 \pm 0.9, 9512.9 \pm 0.9$	0.37 ± 0.10	386 ± 87	-69 ± 29
Mg II	2795.5, 2802.7	$10974.0 \pm 1.4, 11002.2 \pm 1.4$	0.97 ± 0.14	565 ± 66	67 ± 38
[Ne V]	3425.9	13437.0 ± 1.2	1.27 ± 0.11	951 ± 64	-188 ± 27
[O II]	3726.0, 3728.8	$14617.9 \pm 0.8, 14628.8 \pm 0.8$	4.83 ± 0.18	1238 ± 39	-113 ± 16
[Ne III]	3868.7	15180.2 ± 0.8	1.59 ± 0.10	992 ± 45	-67 ± 17
H γ	4340.4	17032.8 ± 2.1	0.84 ± 0.12	844 ± 91	-34 ± 37
[O III]	4363.2	17118.4 ± 0.4	0.47 ± 0.04	327 ± 18	-101 ± 8
[O III]	4958.9	19459.4 ± 0.4	5.18 ± 0.12	1002 ± 17	-42 ± 6
[O III]	5006.8	19647.5 ± 0.4	14.97 ± 0.33	1002 ± 17	-42 ± 6
X-SHOOTER IFU					
Ly α_{15}	1215.7	4768.2 ± 0.3	18.14 ± 0.67	1778 ± 45	-189 ± 18
Ly α_{19}	1215.7	4767.2 ± 0.3	20.81 ± 0.99	1674 ± 42	-250 ± 18
C IV	1548.2, 1550.8	$6076.4 \pm 0.5, 6086.6 \pm 5.8$	5.78 ± 0.32	1372 ± 61	-64 ± 25
He II	1640.4	6438.0 ± 0.5	1.30 ± 0.11	773 ± 51	0 ± 21
C III]	1906.7, 1908.7	$7478.6 \pm 0.6, 7486.7 \pm 0.6$	1.14 ± 0.08	1050 ± 66	-252 ± 24
[O III]	4958.9	19461.2 ± 0.5	8.15 ± 0.16	1030 ± 19	-88 ± 8
[O III]	5006.8	19649.3 ± 0.5	23.56 ± 0.16	1030 ± 19	-88 ± 8
MUSE IFU					
Ly α_{15}	1215.7	4769.4 ± 0.1	18.28 ± 0.50	1572 ± 19	-86 ± 6
Ly α_{19}	1215.7	4769.0 ± 0.1	20.67 ± 1.00	1532 ± 25	-92 ± 7
N V	1238.8, 1242.8	$4860.4 \pm 0.3, 4876.1 \pm 0.3$	0.70 ± 0.04	746 ± 34	-52 ± 18
Si IV	1402.8	5501.0 ± 1.2	0.46 ± 0.05	2244 ± 182	-207 ± 66
N IV]	1483.3, 1486.5	$5825.0 \pm 2.8, 5837.5 \pm 2.8$	0.29 ± 0.09	1785 ± 321	220 ± 142
C IV	1548.2, 1550.8	$6075.6 \pm 0.2, 6085.8 \pm 0.1$	2.88 ± 0.06	1120 ± 16	12 ± 8
He II	1640.4	6435.6 ± 0.2	1.91 ± 0.05	1034 ± 19	0 ± 7
O III]	1660.8, 1666.1	$6512.6 \pm 0.9, 6535.7 \pm 0.9$	0.33 ± 0.04	921 ± 88	-211 ± 40
C III]	1906.7, 1908.7	$7480.6 \pm 0.3, 7488.6 \pm 0.3$	1.21 ± 0.04	1008 ± 32	-60 ± 12
C II]	2325.4, 2326.9	$9119.3 \pm 1.1, 9125.3 \pm 1.1$	0.49 ± 0.04	1445 ± 110	-193 ± 37

4.1.4 Other lines

Other emission lines were fitted with a single Gaussian component. Emission doublets were specified to have equal FWHM, fixed wavelength separation and a fixed flux ratio. For instance, we set the flux ratio N V $\lambda\lambda 1239, 1243$ to 1.1, C III] $\lambda\lambda 1907, 1909$ to 0.66, [Ne IV] $\lambda\lambda 2422, 2424$ to 1.5, [O II] $\lambda\lambda 3726, 3729$ to 1.4 and [O III] $\lambda\lambda 4959, 5007$ to 0.35. In order to obtain a fiducial systemic velocity we use the non-resonant He II $\lambda 1640$ emission line.

4.2 Kinematic maps

From the MUSE data cube, we have extracted the spatially resolved kinematic properties of the UV emission and absorption lines using the fitting procedure outlined in Section 4.1. Due to the relatively low spectral resolution of the MUSE data, we only included a single absorption line in our fit to Ly α , which represents the main absorber.

In Fig. 4, we show the maps of the FWHM, and the velocity offset relative to the He II emission at the position of the UV continuum peak. Figs 12(a) and (b) show the velocity offset for the extended

absorber in Ly α and C IV, respectively. To facilitate consistency checks, we also extracted the kinematic properties of the Ly α , He II and/or C IV from the X-SHOOTER and Keck II long-slit spectra (see Figs A3 and A4).

4.3 Pseudo-narrowband images and line-ratio maps

In order to study the emission-line morphology, we have produced pseudo-narrowband (hereafter, pseudo-NB) images from the MUSE data cube. These images were created by summing pixels along the dispersion axis within spectral windows that include all of the detected line flux: $\lambda_{\text{obs}} = 4705.55\text{--}4718.05, 4722.68\text{--}4726.84, 4734.71\text{--}4740.72, 4742.64\text{--}4754.61$ Å for Ly α aiming to exclude the absorption troughs of the emission line, $\lambda_{\text{obs}} = 5745.74\text{--}5812.24$ for C IV, $\lambda_{\text{obs}} = 6037.49\text{--}6094$ for He II and $\lambda_{\text{obs}} = 6875.09\text{--}6931.81$ for C III]. An image of the adjacent continuum was then subtracted from each, giving a pure emission-line image. The resulting continuum-subtracted, pseudo-NB images are shown on the left of Fig. 4.

Table 3. Best-fitting parameters for the Ly α absorption features, for different instruments. Column (1) gives the redshift for the Ly α emission Gaussian. Column (2) gives the redshift for each Ly α absorption. Column (3) gives the column density ($N_{\text{H I}}$). Column (4) gives the Doppler width b . Column (5) gives the velocity shift of the main absorber with respect to He II emission in the same spectrum. See Table A2 for more results.

Ly α emission redshift (z_{em})	Absorption redshift (z_{abs})	Column density (cm^{-2})	Doppler b parameter (km s^{-1})	Δv (km s^{-1})
X-SHOOTER SLIT				
2.923 03 \pm 0.000 07	2.907 46 \pm 0.000 09	$(9.17 \pm 1.57) \times 10^{13}$	55 \pm 8	- 421 \pm 1
	2.919 17 \pm 0.000 02	$(4.27 \pm 0.20) \times 10^{19}$	52 \pm 1	
	2.927 02 \pm 0.000 06	$(8.06 \pm 0.70) \times 10^{13}$	142 \pm 9	
	2.933 01 \pm 0.000 04	$(2.30 \pm 0.30) \times 10^{13}$	35 \pm 5	
2.923 60 \pm 0.000 07	2.907 47 \pm 0.003 11	$(8.09 \pm 1.66) \times 10^{13}$	48 \pm 9	- 422 \pm 2
	2.919 15 \pm 0.000 01	$(1.52 \pm 0.12) \times 10^{15}$	153 \pm 4	
	2.926 72 \pm 0.000 02	$(6.39 \pm 0.73) \times 10^{13}$	142 \pm 12	
	2.933 04 \pm 0.000 01	$(1.95 \pm 0.30) \times 10^{13}$	31 \pm 5	
X-SHOOTER IFU				
2.921 65 \pm 0.000 24	2.906 43 \pm 0.000 03	$(3.15 \pm 2.51) \times 10^{14}$	54 \pm 17	- 533 \pm 4
	2.917 77 \pm 0.000 06	$(3.46 \pm 0.50) \times 10^{19}$	52 \pm 2	
	2.925 25 \pm 0.000 12	$(1.95 \pm 0.63) \times 10^{13}$	40 \pm 13	
	2.931 78 \pm 0.000 10	$(1.84 \pm 0.76) \times 10^{13}$	23 \pm 10	
2.922 26 \pm 0.000 24	2.906 43 \pm 0.000 15	$(3.16 \pm 0.14) \times 10^{14}$	51 \pm 19	- 600 \pm 6
	2.917 78 \pm 0.000 03	$(1.86 \pm 0.65) \times 10^{15}$	136 \pm 12	
	2.925 22 \pm 0.000 12	$(1.58 \pm 0.58) \times 10^{13}$	34 \pm 13	
	2.931 78 \pm 0.000 10	$(1.66 \pm 0.75) \times 10^{13}$	22 \pm 10	
MUSE IFU				
2.922 91 \pm 0.000 10	2.906 92 \pm 0.000 20	$(1.13 \pm 0.23) \times 10^{14}$	67 \pm 32	- 434 \pm 6
	2.918 43 \pm 0.000 08	$(3.50 \pm 0.39) \times 10^{19}$	50 \pm 3	
	2.927 14 \pm 0.000 18	$(2.76 \pm 1.04) \times 10^{13}$	114 \pm 40	
	2.931 92 \pm 0.000 21	$(2.69 \pm 0.83) \times 10^{13}$	92 \pm 39	
2.923 24 \pm 0.000 08	2.906 86 \pm 0.000 32	$(9.27 \pm 3.44) \times 10^{13}$	60 \pm 21	- 442 \pm 2
	2.918 58 \pm 0.000 02	$(1.06 \pm 0.07) \times 10^{15}$	175 \pm 6	
	2.926 66 \pm 0.000 20	$(1.77 \pm 0.76) \times 10^{13}$	88 \pm 51	
	2.932 07 \pm 0.000 33	$(1.54 \pm 0.67) \times 10^{13}$	55 \pm 41	

Note. The He II emission line was outside the spectral range covered by the red arm of VLT UVES and thus we do not give the velocity shift for this instrument.

Table 4. Best-fitting parameters for the C IV absorption features, for different instruments. Column (1) gives the redshift for the C IV emission Gaussian. Column (2) gives the redshift for each C IV absorption. Column (3) gives the column density ($N_{\text{C IV}}$). Column (4) gives the Doppler width b . Column (5) gives the velocity shift of the main absorber with respect to He II emission in the same spectrum. See Table A3 for more results.

C IV emission redshift (z_{em})	Absorption redshift (z_{abs})	Column density (cm^{-2})	Doppler parameter (km s^{-1})	Δv (km s^{-1})
X-SHOOTER SLIT				
2.924 66 \pm 0.000 30	2.919 65 \pm 0.000 11	$(3.65 \pm 0.53) \times 10^{14}$	114 \pm 14	- 384 \pm 8
X-SHOOTER IFU				
2.924 79 \pm 0.000 33	2.919 21 \pm 0.000 31	$(6.19 \pm 1.27) \times 10^{14}$	62 \pm 7	- 491 \pm 9
MUSE IFU				
2.924 27 \pm 0.000 10	2.919 27 \pm 0.000 04	$(3.14 \pm 0.18) \times 10^{14}$	100 \pm 7	- 371 \pm 3

Note. The He II emission line was outside the spectral range covered by the red arm of VLT UVES and thus we do not give the velocity shift for this instrument.

Our flux-ratio maps use the flux maps produced by our line fitting procedure (Sections 4.1 and 4.2), and we have simply divided one line flux map by another (see Fig. 6).

4.4 Ionization models

To assist in understanding the physical conditions and nature of the extended line emitting gas of the radio galaxy, a grid of photoioniza-

tion models (see Figs 7–10) were computed using the multipurpose code MAPPINGS IIE (Binette, Dopita & Tuohy 1985; Ferruit et al. 1997).

Our model grid contains two possible values for the ionizing spectral index, $\alpha = -1.5$ with a high-energy cut-off of 5×10^4 eV, and $\alpha = -1.0$ with a high energy cut-off of 1×10^3 eV. The gas chemical abundances were varied between $0.5 Z_{\odot}$ and $3.0 Z_{\odot}$ (with Z_{\odot} being the solar metallicity), with all metals being scaled linearly with O/H except for nitrogen. The nitrogen abundance was varied such that $\text{N}/\text{H} \propto \text{O}/\text{H}$ at $Z/Z_{\odot} < 0.3$ and $\text{N}/\text{O} \propto \text{O}/\text{H}$ at Z/Z_{\odot}

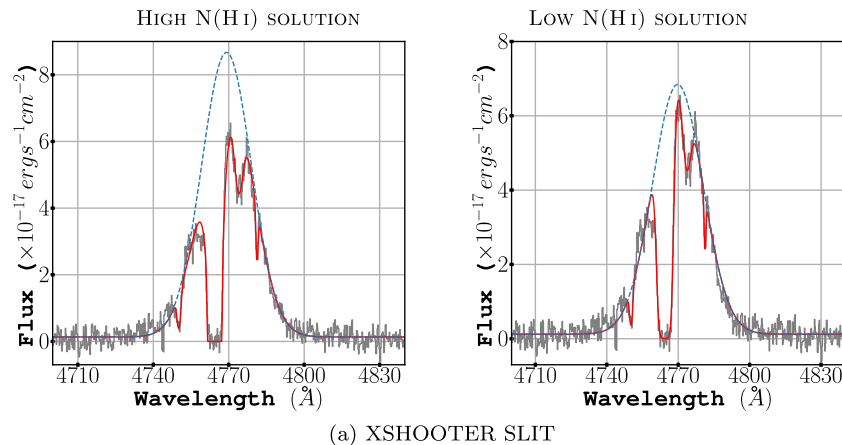


Figure 1. Ly α profile of MRC 0943–242 extracted from the X-SHOOTER long slit, with the Gaussian emission component (dashed blue line) plus absorption model overlaid (red line). The left and right columns show the high and low column density best fitting, respectively. See other instruments in Fig. A1.

≥ 0.3 , to take into account its expected secondary behaviour at moderate-to-high metallicity (e.g. Villar-Martín et al. 1999; Henry, Edmunds & Köppen 2000). We adopt the Solar chemical abundances of Asplund, Grevesse & Jacques Sauval (2006). The ionization parameter³ varies from $U = 10^{-4}$ to 1.6. For all models, we use hydrogen density of 100 cm^{-3} and adopt a single-slab, ionization-bounded, isochoric geometry.

Because MRC 0943–242 is a powerful radio galaxy, it is plausible that the radio jets drive ionizing shocks into the interstellar medium (ISM). Thus, we also make use of shock and shock plus precursor models from the literature, computed by Allen et al. (2008) using MAPPINGS III. The models used consist of one sequence in which the emission comes solely from shock-heated gas, while the other sequence is a combination of shock-heated gas and a photoionized precursor. In order to be as consistent as possible with our MAPPINGS I E photoionization models, we have selected sequences with solar abundance, shock velocities covering the range $v_s = 100$ up to 1000 km s^{-1} in steps of 25 km s^{-1} , hydrogen density $n_H = 100 \text{ cm}^{-3}$ and magnetic field $B = 100 \mu\text{G}$.

The large number of emission lines now detected from this radio galaxy makes it challenging to diagnose the physical conditions using only diagnostic diagrams. For this reason, we have written a simple PYTHON code that searches the assembled grid of ionization models to find the model that best reproduces an ensemble of emission line ratios. The routine includes extinction A_V as a free parameter, and we have assumed $R_V = 3.1$ and the dust extinction curve of Fitzpatrick (1999). For this we use all possible line ratios formed using lines detected in our X-SHOOTER long-slit spectrum, with the exception of ratios involving Ly α , where transfer effects are likely to be strong. All line ratios included in this analysis are given equal weighting, and the goodness of fit is evaluated using reduced chi-square (χ_ν^2).

³ The ionization parameter U is defined as the ratio of ionizing photons to hydrogen atoms and its expression is $Q/(4\pi r^2 n_H c)$, with Q as the ionizing photon luminosity of the source, r is the distance of the cloud from the ionizing source, n_H is the hydrogen density and c is the speed of light.

5 RESULTS AND DISCUSSION

5.1 Radio-mode feedback

In Fig. 4, we show maps of the flux and kinematic properties of the lines Ly α , C IV, He II and C III] from our analysis of the MUSE data cube, with the position of the nucleus and the radio hotspots marked. To supplement the MUSE results, we also show kinematic results from our single-slit observations from X-SHOOTER and Keck II in Figs A3 and A4, respectively. Taking into account differences in spatial resolution, spectral resolution and slit position between the different observations, we find good consistency between the kinematic results from the MUSE, X-SHOOTER and Keck II data sets.

The pseudo-NB images show an extended emission-line halo with a major axis that is well aligned with the PA of the radio source (see also Gullberg et al. 2016), similar to the close alignment found by Pentericci et al. (1999, 2001) using broad-band *HST* images of this object.

In agreement with previous kinematic studies of this galaxy (Villar-Martín et al. 2003; Humphrey et al. 2006), we find that the extended emission-line halo shows a central, extended region of kinematically turbulent gas with relatively high FWHM ($\gtrsim 800 \text{ km s}^{-1}$) that almost reaches the radio hotspots, with kinematically more quiescent gas ($\lesssim 800 \text{ km s}^{-1}$) located at larger radii. In addition, we find the most extreme gas kinematics within ~ 1 arcsec of the position of the west radio hotspot, with all of these lines showing their highest FWHM and greatest relative blueshift there. Along the Keck II PA, the FWHMs of both C IV and He II show a modest increase from the nucleus towards the radio hotspots, but peaking ~ 0.6 arcsec short and sharply falling to smaller FWHM values.

Our velocity maps (Fig. 4) and velocity curves (see Figs A3 and A4) show that the central, kinematically perturbed gas shows the most redshifted velocities, with a dramatic transition to blueshifted velocities taking place near the positions of the radio hotspots. At the position of the west radio hotspot, spatially coincident with the largest measured FWHM, we find the highest relative blueshift ($\gtrsim 300 \text{ km s}^{-1}$) in Ly α , C IV, He II and C III].

Thus, there is clear evidence for jet gas interactions strongly affecting the kinematic properties of the extended emission-line gas (see Fig. A5). However, the precise nature of this interaction is not immediately clear. Whereas our data only give us the line-of-sight

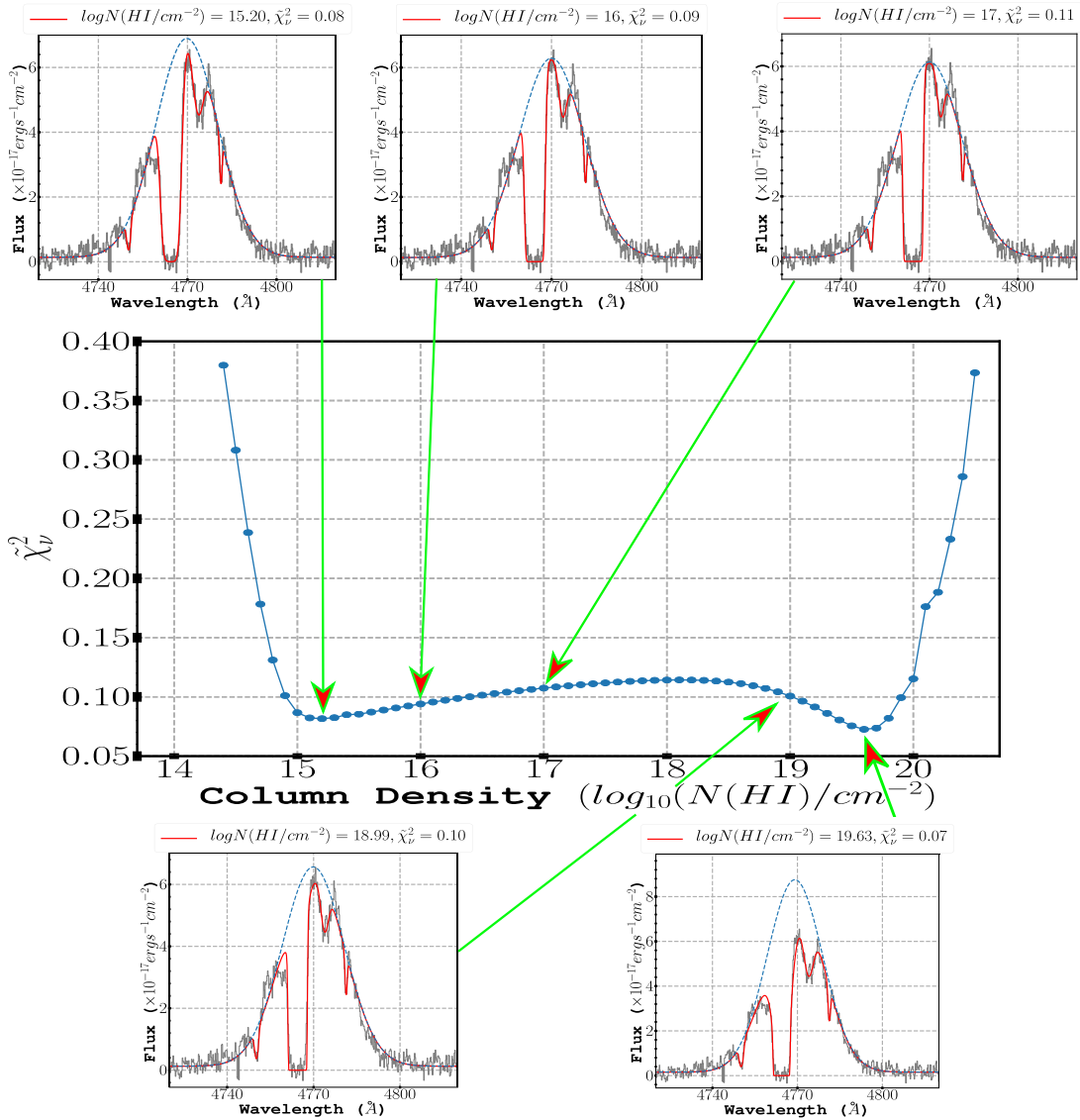


Figure 2. Plot of column density ($N(\text{HI})$) versus reduced chi-square ($\tilde{\chi}_r^2$), showing the presence of two widely spaced ‘best fitting’, between which lie a broad range of inferior, but nonetheless reasonable fits. Data points other than the two ‘best fitting’ were produced by running our fitting code with $N(\text{HI})$ fixed to specific values. Around the main plot we show selected fits to the X-SHOOTER long-slit Ly α profile, to further illustrate how the fits evolve as a function of $N(\text{HI})$.

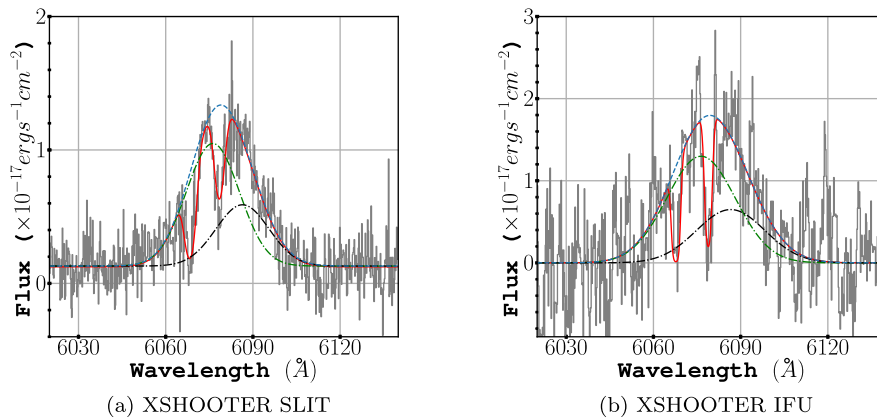


Figure 3. The C IV profile of MRC 0943–242, with the Gaussian emission component (dashed blue line) and emission plus absorption model overlaid (red line). The two individual doublet components are also shown. See the C IV profile from other telescopes/instruments in Fig. A2.

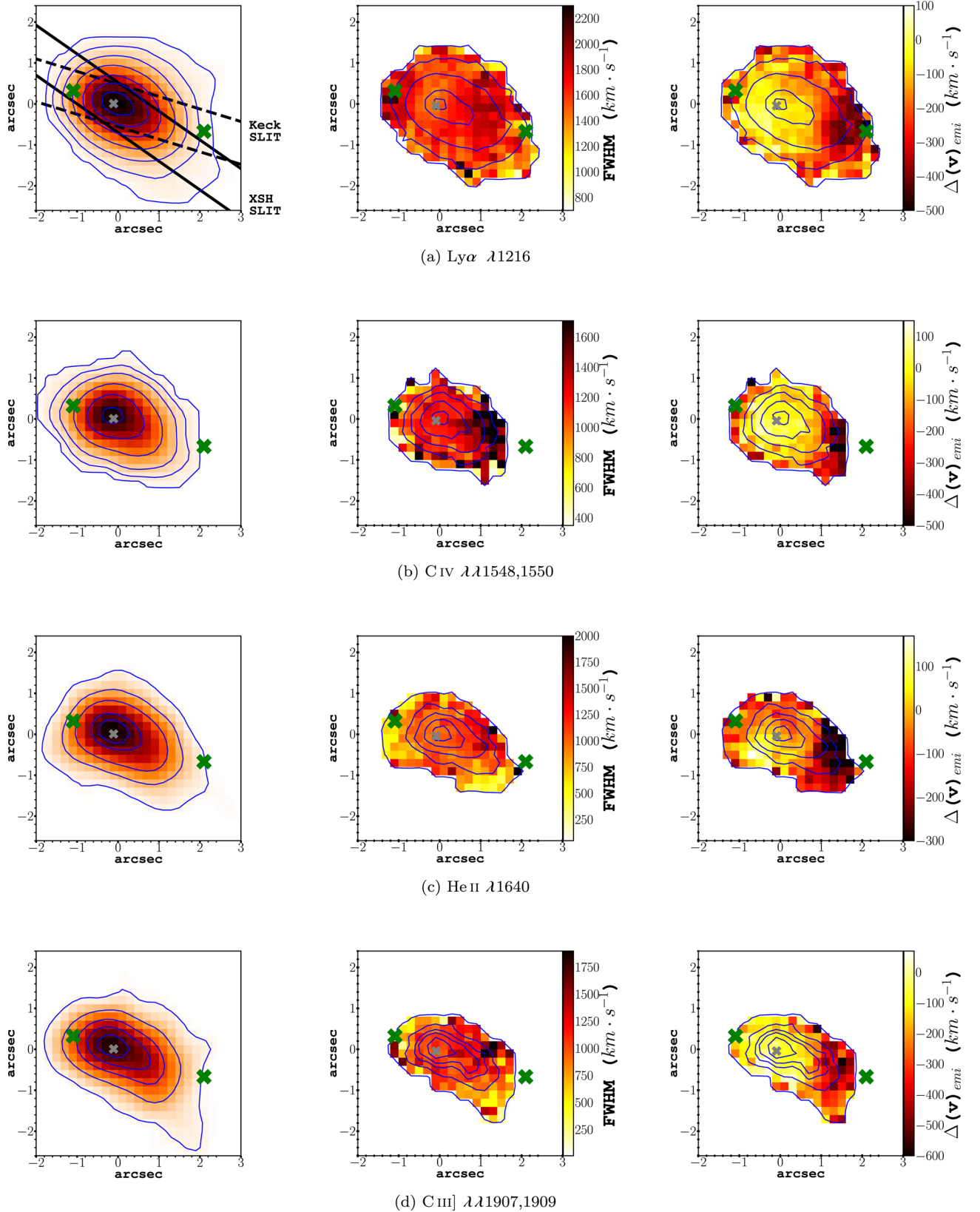


Figure 4. From left to right, we show the pseudo-narrowband images, the FWHM map and the velocity map. The pseudo-narrowband image of $\text{Ly}\alpha$ is overlaid with the position of the X-SHOOTER slit (solid lines) and KECK slit (dashed lines). Contour levels: $\text{Ly}\alpha - (0.3, 1.3, 3.8, 12.5, 16.8) \times 10^{-16}$, $\text{C IV} - (0.5, 1.0, 2.0, 3.5, 4.3) \times 10^{-16}$, $\text{He II} - (0.1, 0.8, 1.0, 1.5, 2.0) \times 10^{-16}$ and $\text{C III]} - (0.08, 0.5, 0.8, 1.0, 1.3) \times 10^{-16} \text{ erg cm}^{-2} \text{ s}^{-1} \text{ arcsec}^{-2}$. The green 'X' represents the positions of the radio hotspots. The coordinate (0,0) corresponds to the assumed position of the AGN that is marked with a grey 'x'. The scale of $5 \text{ arcsec} \times 5 \text{ arcsec}$ on the axes corresponds to the physical scale of $40 \text{ kpc} \times 40 \text{ kpc}$.

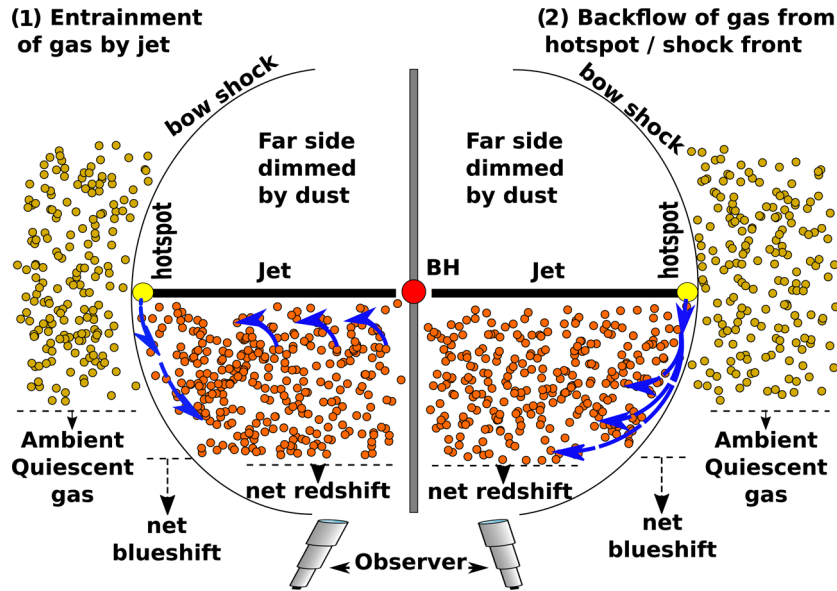


Figure 5. Here, we show two simple scenarios to explain the emission-line kinematics in MRC 0943–242. (1) The relativistic radio jets are produced in the central active nucleus and propagate outward through the host galaxy, terminating in a hotspot that represents the working surface of the jet against the ambient ISM. The radio plasma cools and diffuses/flows laterally away from the hotspot, carrying with it condensations of warm ionized gas that are then seen as localized blueshifted line emission with relatively large FWHM, closely associated with the hotspots. Beyond the radio cocoon, the ambient ISM remains untouched by the jets and thus shows relatively narrow emission lines. The jets entrain gas from the ISM of the galaxy, dragging gas in towards the jet as well as along the velocity vector of the jet. The inward motion of the entrained gas results in a net redshift when the radio jet axis is viewed side-on. (2) As above, but with a backflow of material away from the head of the radio jet, instead of entrainment, producing the observed redshifting of the kinematically perturbed gas. In both cases, the ISM would need to contain a significant quantity of dust, to dim the emission from gas on the far side of the galaxy.

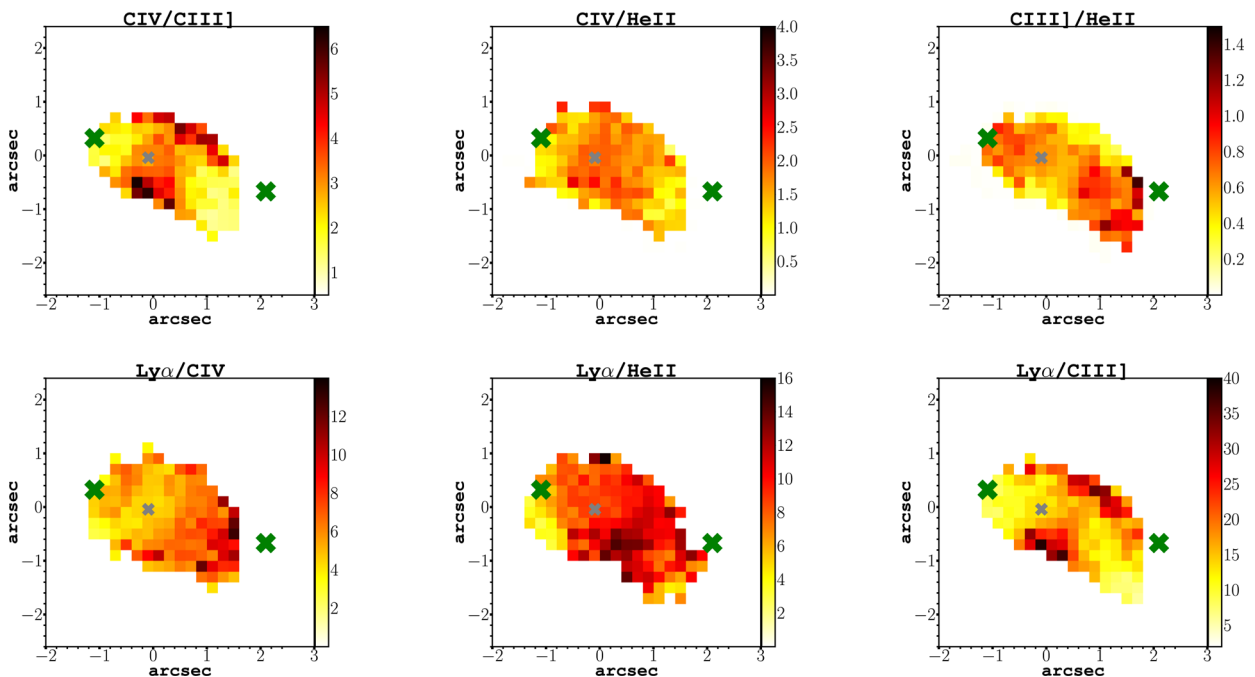


Figure 6. Flux-ratio maps of the MRC 0943–242. See the text for a detailed description of the flux-ratio maps. The most remarkable feature in these maps is that the gas close to the locations of the hotspots appears clearly differentiated in several maps, such as $C\text{IV}/C\text{III}]$, $C\text{IV}/\text{HeII}$, $C\text{III}]/\text{HeII}$ and $\text{Ly}\alpha/C\text{III}]$. The green ‘X’ represent the positions of the radio hotspots and the grey ‘x’ the position of the AGN.

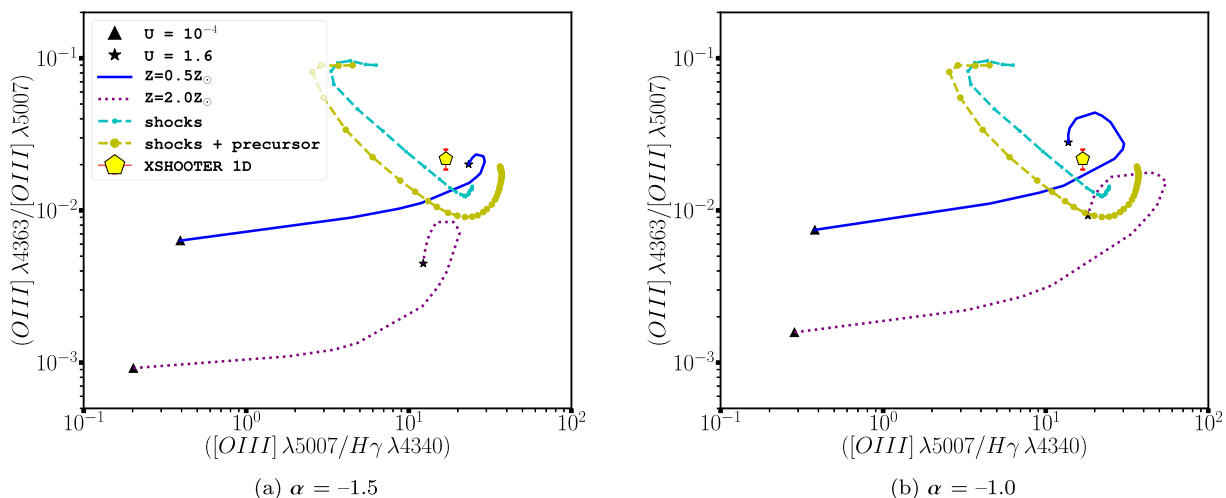


Figure 7. Comparison of the observed emission line ratios using integrated spectra from the X-SHOOTER long-slit (yellow pentagon) with photoionization ($0.5Z_{\odot}$ sequence is represented by the solid blue line and the $2.0Z_{\odot}$ sequence by the purple dotted line), pure shock models (blue solid circles connected by a dashed line) and the composite shock + precursor models (large yellow solid circles connected by a dashed line). In the case of the photoionization models, we use ionizing continuum power-law index $\alpha = -1.5$ (left-hand side) or $\alpha = -1.0$ (right-hand side). At the end of each sequence, a solid black triangle corresponds to the initial value of the ionization parameter ($U = 10^{-4}$) and a solid black star that corresponds to the maximum value of the ionization parameter ($U = 1.6$). The pure shock and the composite shock + precursor models are from Allen et al. (2008). Both shock model sequences are characterized by hydrogen density 100 cm^{-3} , magnetic field $100 \mu\text{G}$ and velocity covering the range $v_s = 100$ up to 1000 km s^{-1} .

velocity, the radio jet motion is likely to be close to the plane of the sky.

Naively, one might have expected the perturbed gas at radii smaller than the hotspots to be in outflow from the galaxy, and thus blueshifted relative to the ambient quiescent gas. However, with the notable exception of a localized region of gas associated with the west hotspot, the vast majority of the perturbed gas shows a relative *redshift* with respect to the quiescent gas. In addition, we find that the quiescent gas that lies beyond the highly perturbed, inner regions shows a net blueshift, a feature that is seen on the east and west sides of the object, in both C IV and He II .

In Fig. 5, we illustrate two scenarios that may explain the remarkable kinematic properties observed in MRC 0943–242. In both cases, the relativistic jets of radio plasma are produced in the central active nucleus and propagate outward through the host galaxy, terminating in a hotspot that represents the working surface of the jet against the ambient ISM. Upon reaching the hotspot, the radio plasma cools and diffuses/flows laterally away from the hotspot, carrying with it condensations of warm ionized gas that are seen as localized blueshifted line emission with relatively large FWHM, closely associated with the hotspots. Beyond the radio cocoon, the ambient ISM remains untouched by the radio jets and thus shows relatively narrow emission lines. Within this general framework, the fact that much of the kinematically perturbed gas is *redshifted* suggests that we are witnessing the inflow of gas driven by radio-mode feedback, due to (1) gas being pulled in towards the radio jets as part of the entrainment process; or (2) a backflow of material from the radio hotspots that cycles material back into the host galaxy. An interesting implication of the second scenario is that, judging by the fact that this perturbed and blueshifted component dominates the overall line emission from within the radius of the radio source, a significant quantity of gas is funnelled back towards the host galaxy after being entrained/accelerated by the radio jets.

Although the long-term effect of the radio-loud activity may well be to quench star-formation (hereafter SF) and starve the AGN of fuel, we speculate that MRC 0943–242 may be in a phase of *positive*

radio-mode feedback where fuel is cycled back into the central regions of the galaxy to form stars and fuel the AGN. Indeed, a number of studies have found a correlation between small radio-jets and a relatively higher SF rate (e.g. Humphrey et al. 2006, 2011), and this HzRG appears to have a substantial rate of SF in the range $200\text{--}1400 \text{ M}_{\odot} \text{ yr}^{-1}$ (Gullberg et al. 2016; see also Humphrey et al. 2006).

The two scenarios described above are not necessarily mutually exclusive; it seems plausible that both could operate simultaneously. In either case, we point out that the ISM would need to contain dust so as to dim the perturbed gas located on the far side of the galaxy from the observer, suggesting that significant quantity of dust is able to survive the shocks driven into the ISM during the passage/growth of the radio source through the host galaxy, consistent with the detection of significant UV continuum polarization (Vernet et al. 2001).

Maps of several important UV line ratios are shown in Fig. 6 (see also Fig. A6). The large variation of $\text{C IV}/\text{C III}$ in our map suggests there is a substantial range in ionization level across the object. In addition, we find a spatial correlation between the radio hotspots and several of the emission line ratios, with relatively low values of $\text{C IV}/\text{He II}$ and $\text{C IV}/\text{C III}$, and high values of $\text{C III}/\text{He II}$, spatially associated with both radio hotspots, and qualitatively consistent with lower U in the vicinity of the hotspots.

The $\text{Ly}\alpha/\text{He II}$ ratio shows no direct spatial correlation with the positions of the radio hotspots. However, we do find relatively low values for this ratio ($\lesssim 6$) to the immediate east of the eastern radio hotspot and ~ 0.9 arcsec south of the western hotspot, in both cases spatially coincident with a region of kinematically quiescent gas as seen in the He II and C III kinematic maps (Fig. 4), suggesting that the $\text{Ly}\alpha$ escape fraction is much lower in regions that are unaffected by radio-mode feedback. Scenarios that may explain this result include: (i) reduction of dust in the kinematically perturbed regions due to jet-driven shocks (e.g. Villar-Martín et al. 2001); (ii) greater velocity overlap between emitting and absorbing gas phases in the kinematically quiescent regions (e.g. Tenorio-Tagle

et al. 1999) and (iii) the presence of an optically thick shell of gas encasing the expanding radio cocoon (e.g. Binette et al. 2006). The ionization/excitation and metallicity of the extended gas will be examined in greater detail in Section 5.2.

5.2 Ionization and metallicity of the extended emission-line gas

Our X-SHOOTER spectrum of MRC 0943–242 covers a wide range of wavelength and contains numerous emission lines from various species, making it particularly useful for studying the ionization and chemical abundances in the extended ionized gas. From our ionization model grid (see Section 4.4), the single model that provides the best overall fit to the X-SHOOTER emission-line spectrum is a photoionization model with $U = 0.018$, $\alpha = -1.0$ and gas metallicity $Z/Z_{\odot} = 2.1$. In addition, our best-fitting model has $A_V = 0$. Table 5 shows the X-SHOOTER emission lines normalized to the flux of $\text{He II } \lambda 1640$. Our best-fitting model parameters are generally consistent with conclusions obtained from smaller subsets of the UV lines by previous authors (Vernet et al. 2001; Humphrey et al. 2008a; Gullberg et al. 2016).

Although the reduced chi-square is reasonably small ($\chi^2_{\nu} = 2.75$) and many line ratios are well reproduced by the model, a number of other line ratios are not well reproduced. In particular, the model produces too low a value of $[\text{O III}] \lambda 4363/[\text{O III}] \lambda 5007$ (see Fig. 7), indicating that T_e is too low in the model. This could be due to the presence of some shock-heating in the extended gas in addition to the dominant AGN-photoionized gas (see also Tadhunter, Robinson & Morganti 1989), as also suggested by Gullberg et al. (2016) based on the strength of $\text{C II}]$ relative to C IV , $\text{C III}]$ and He II in the integrated MUSE spectrum.

In addition, we notice that $\text{O VI} + \text{C II}$, $[\text{O II}]$ and $\text{C II}]$ are under-predicted in the model relative to our measurements, suggesting the presence of clouds with a substantial range in U within the extended gas sampled by our X-SHOOTER spectrum (e.g. Humphrey et al. 2008a).

The best-fitting model also produces an $\text{H } \gamma/\text{He II } \lambda 1640$ ratio that is significantly below the observed value. This suggests that the ionizing spectral energy distribution (SED) ($\alpha = -1.0$) may be too hard, or that reddening, for which we have no reliable diagnostic, may be important in this object.

To supplement our analysis and partially illustrate the above results, we also show selected diagnostic diagrams (Figs 7, 8 and 9).

In order to study the spatial variation of the UV emission line ratios, we show in Figs 10 and 11 several diagnostics diagrams with UV line ratios measured from the individual spaxels in the MUSE data cube. In these diagrams, we use line ratios involving $\text{Ly } \alpha$, C IV , He II and $\text{C III}]$ only, due to the narrower spectral range of MUSE and the lower chance of detecting the faint lines in the individual spaxels.

The MUSE spaxels show a substantial dispersion in each of the diagrams (Figs 10 and 11), with a ‘centre of gravity’ that corresponds approximately with the position of the X-SHOOTER data point (yellow pentagon).

The distribution of data points in diagrams involving only C IV , He II and $\text{C III}]$ is qualitatively consistent with a range in U . Of these ratios, $\text{C IV}/\text{C III}]$ is likely to be the most reliable indicator of U , and given its large variation (~ 0.6 dex) we conclude that there is likely to be a large variation in U (or ionization state) throughout the extended ionized halo, as suggested by our analysis of the 1D X-SHOOTER spectrum above. However, we note that exploring the spatial variation in metallicity and ionization parameter using the X-SHOOTER spectrum with a different aperture (2.1 arcsec) has

only a minor effect on these parameters. From our ionization model grid, we find that the single model that provides the best overall fit to the new aperture shows metallicity and ionization parameter affected by changes < 15 per cent when compared with that obtained with a smaller aperture (0.8 arcsec; see Tables 5 and A4).

We also note the presence of significant scatter perpendicular to the U -sequence loci [see the flux-ratio maps (Fig. 6) plotted on the diagrams in Figs 10 and 11]. We suggest this may be due to metallicity inhomogeneities or local differences in the hardness or source of ionization.

The spaxels with relatively low values of $\text{C IV}/\text{C III}]$ (black circles), which are also relatively close to the radio hotspots, clearly have different ionization conditions to the rest of the nebula, but degeneracies between models make it challenging to determine the origin of this difference. Although they are consistent with having among the lowest values of U , these spaxels are also close to the shock model loci. Thus, we suggest that the radio source induces a lower ionization parameter where it most strongly interacts with the ISM, perhaps due to compression of gas, or that shock ionization contributes significantly in these specific regions of the $\text{Ly } \alpha$ halo.

The $\text{Ly } \alpha/\text{He II}$ values show a dispersion within the nebula (~ 0.6 in dex), with most points having lower values than the minimum values produced by the plotted photoionization or shock models. This is likely due to a varying impact of transfer effects across the nebula, but it is not clear whether the observed $\text{Ly } \alpha$ flux is being suppressed by resonant scattering due to dust or due to redirection of photons into other lines of sight. Interestingly, the locus of photoionization models using $\alpha = -1.0$ and $Z/Z_{\odot} = 2.0$ passes through the cloud of MUSE points in the $\text{C IV}/\text{C III}]$ versus $\text{Ly } \alpha/\text{He II}$ diagram, suggesting that the systematically low $\text{Ly } \alpha/\text{He II}$ ratios of MRC 0943–242 may be partly due to a relatively hard ionizing SED and relatively high gas metallicity. Unlike the other UV ratios, we find no correlation between $\text{Ly } \alpha/\text{He II}$ and proximity to the radio hotspots.

5.3 Nature of the extended H I Absorber

5.3.1 H column density

One of the key findings from our analysis of the $\text{Ly } \alpha$ velocity profile of MRC 0943–242 is the strong degeneracy between the column density ($N(\text{H I})$) and the Doppler width (b) of the main absorber, with a broad range in $N(\text{H I})$ yielding a reasonable fit to the data, and with the best fitting located near each end of this range: $\log N(\text{H I}/\text{cm}^{-2}) = 15.20$ and 19.63 . The latter value is in agreement with the fits obtained in previous studies of MRC 0943–242 (e.g. Röttgering et al. 1995; Binette et al. 2000; Jarvis et al. 2003; Gullberg et al. 2016). None of the previous studies identified the N-b degeneracy or the second, low column density fit. Clearly, this degeneracy has implications for our understanding of the properties of the absorbing gas, where they are derived from $N(\text{H I})$.

As argued by previous authors, detection of C IV in the main absorber indicates that the gas is at least partially ionized and contains some metal-enriched gas, but the column ratio between C IV with H I does not allow a straightforward determination of the ionization structure or metallicity of the gas (e.g. Binette et al. 2000; Jarvis et al. 2003). In addition, we can calculate a lower limit on the total H column density by assuming $N_{\text{C}} \geq N_{\text{C IV}}$ and appropriate limits for the column ratio $N_{\text{C}}/N_{\text{H}}$. Assuming $N_{\text{C}} \geq N_{\text{C IV}}$ and $\text{C}/\text{H} \leq 3$ times Solar, we obtain $N_{\text{H}} \gtrsim 5 \times 10^{17} \text{ cm}^{-2}$. Note that this limit is not dependent on the value of $N(\text{H I})$.

Table 5. Comparison of model line ratios with observed line ratios. Column (1): emission line ratios; column (2): observed X-SHOOTER line fluxes normalized by He II $\lambda 1640$; column (3): parameters and relative line fluxes produced by our best-fitting MAPPINGS model; column (4): our best-fitting model using $\alpha = -1.5$ instead of $\alpha = -1.0$; column (5): parameters and relative line fluxes produced by our best-fitting shock models; and column (6) shock + precursor models extracted from Allen et al. (2008).

Line ratios (1)	Obs. flux (2)	Model 01 (3)	Model 02 (4)	Model 03 (5)	Model 04 (6)
		$U = 0.018$ $\alpha = -1.0$ $Z/Z_{\odot} = 2.1$ $\chi_{\nu}^2 = 2.75$	$U = 0.032$ $\alpha = -1.5$ $Z/Z_{\odot} = 1.2$ $\chi_{\nu}^2 = 4.66$	shocks $v = 225 \text{ km s}^{-1}$ $Z/Z_{\odot} = 1.0$ $\chi_{\nu}^2 = 7.15$	shock + prec. $v = 725 \text{ km s}^{-1}$ $Z/Z_{\odot} = 1.0$ $\chi_{\nu}^2 = 6.53$
Ly α^a /He II	9.90 ± 0.43	11.30	16.56	59.15	28.50
(O VI+C II)/He II	0.77 ± 0.12	0.31	0.24	4.90	5.70
N V/He II	0.30 ± 0.06	0.39	0.21	3.01	0.69
C IV/He II	1.47 ± 0.11	2.14	2.05	6.99	1.48
C III]/He II	0.54 ± 0.04	1.24	1.01	1.68	2.21
C II]/He II	0.27 ± 0.05	0.17	0.08	1.13	2.33
[Ne IV]/He II	0.18 ± 0.05	0.43	0.31	1.00	1.51
Mg II/He II	0.56 ± 0.08	0.50	0.45	2.81	3.58
[Ne V]/He II	0.64 ± 0.06	0.58	0.43	0.48	0.49
[O II]/He II	2.79 ± 0.15	0.93	0.46	3.45	1.10
[Ne III]/He II	1.06 ± 0.08	0.69	0.64	1.03	1.12
H γ /He II	0.50 ± 0.10	0.17	0.31	0.84	0.44
[O III]4363/He II	0.19 ± 0.02	0.11	0.09	0.20	0.68
[O III]5007/He II	8.49 ± 0.33	8.79	8.45	2.90	0.95

Note. ^aLy α was not used in the fitting.

Table 6. Low-ionization absorption lines extracted from the Keck II spectrum at the redshift of the main absorber. Column (1): absorption lines; column (2): rest-frame wavelength; column (3): oscillator strength; column (4): rest-frame equivalent width; and column (5): column density.

Line (1)	$\lambda_{\text{rest}} (\text{\AA})$ (2)	f (3)	$W_{\text{rest}} (\text{\AA})$ (4)	$N (\text{cm}^{-2})$ (5)
O I	1302.2	0.05	<5	$<1.5 \times 10^{15}$
C I	1277.2	0.10	<4	$<8.0 \times 10^{14}$
C I	1328.8	0.06	<3	$<8.2 \times 10^{14}$
C I	1560.3	0.08	<2	$<3.0 \times 10^{14}$
C I	1656.9	0.14	<2	$<1.5 \times 10^{14}$
C II	1334.5	0.13	<4	$<5.0 \times 10^{14}$

5.3.2 Ionization structure and metallicity

To obtain additional constraints on its chemical and ionization properties, we have searched our deep Keck II spectrum for low-ionization absorption lines at the redshift of the main absorber. Our analysis has not revealed any detection of additional absorption lines, and we show the most relevant 3σ upper limits in Table 6. To convert equivalent width W_{λ} to column density N , we use

$$N = \frac{1.13 \times 10^{20} W_{\lambda,0}}{f \lambda_0^2} \text{ cm}^{-2}, \quad (1)$$

where f is the oscillator strength, $W_{\lambda,0}$ is the rest-frame equivalent width (in \AA) and λ_0 is the rest-frame wavelength of the line (in \AA) (e.g. Humphrey et al. 2013a).

Interestingly, the fact that N_{CIV} is at least twice N_{CI} indicates that the gas is mostly ionized, while $N_{\text{CII}}/N_{\text{CIV}} \lesssim 1.3$ indicates that the ionized zone itself is highly ionized. By extension, hydrogen is also likely to be mostly ionized, with the total H column density likely to be more than three times that of H I, independently of which value of N_{HI} we adopt.

Provided the H I absorption is dominated by gas in a neutral zone, it can then be assumed that $N_{\text{CI}}/N_{\text{HI}} \sim \text{C}/\text{H}$ and $N_{\text{OI}}/N_{\text{HI}} \sim \text{O}/\text{H}$, which would allow constraints to be placed on the gas chemical abundances. In the extreme case, where $N_{\text{HI}} = 4.3 \times 10^{19} \text{ cm}^{-2}$, we would then obtain abundance ratios $\text{C}/\text{H} \lesssim 0.013 Z_{\odot}$ and $\text{O}/\text{H} \lesssim 0.076 Z_{\odot}$, meaning the absorber would be extremely metal poor. Conversely, if the H I absorption is due to gas in an ionized zone with low, but non-negligible H I fraction, i.e. if the absorber is ‘matter bounded’, then the assumption that $N_{\text{CI}}/N_{\text{HI}} \sim \text{C}/\text{H}$ and $N_{\text{OI}}/N_{\text{HI}} \sim \text{O}/\text{H}$ does not necessarily hold.

5.3.3 Size, shape and mass

The most likely geometry for the main absorber is a shell or bubble of gas surrounding the host galaxy and at least part of its Ly α emitting halo (Binette et al. 2000). The simplest way to obtain a lower limit to the radius of the absorbing structure is to determine the maximum observed offset between the projected position of the nucleus, and the most distant pixel or spaxel where the absorber is detected. Measuring from the MUSE data cube, Gullberg et al. (2016) obtained a maximum offset from the nucleus of $\gtrsim 60 \text{ kpc}$, and we adopt this value as a lower limit to the radius of the shell.

In Fig. 12(a), we show a map of the line-of-sight velocity of the main H I absorber, measured from the MUSE data. The absorption feature shows a gradient in velocity, with a significant decrease in blueshift outward from the (projected) central region of the galaxy (see also Fig. A3). The presence of this trend is independent of whether we adopt the $\log N(\text{H I}/\text{cm}^{-2}) = 15.20$ or 19.63 fit to the H I absorber. Similarly, the C IV absorption doublet also appears to show a radial decrease in its blueshift (Fig. 12b). This result is consistent with what one would expect if the absorber is an expanding shell centred on the radio galaxy: At larger projected distances from the centre, the bulk velocity vector of the shell material is at a larger inclination to the line of sight, and thus appears to be less blueshifted. As a consistency check on the radius of the shell, we

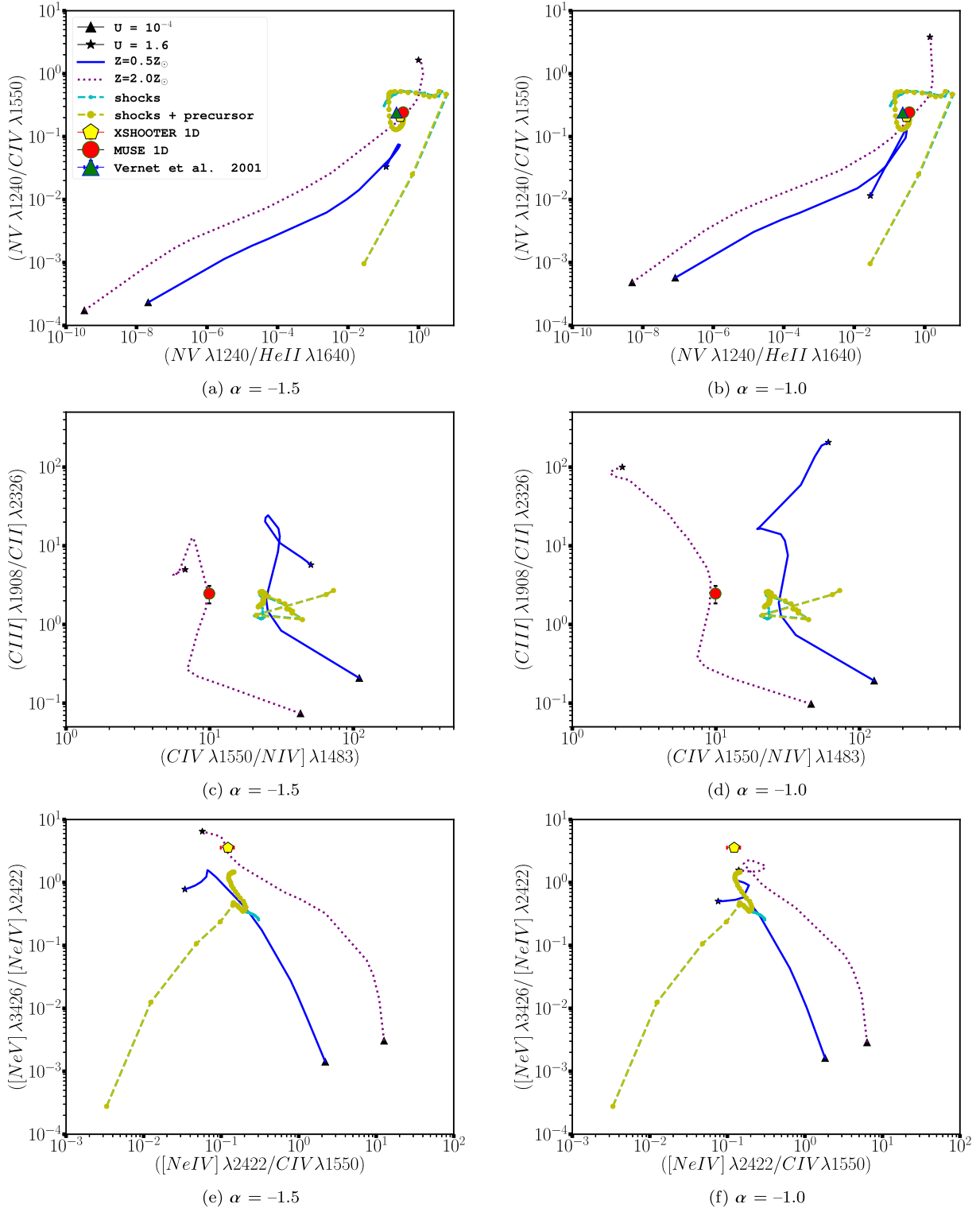


Figure 8. Comparison of the observed emission line ratios using integrated spectra from the MUSE IFU (red circle), X-SHOOTER long-slit (yellow pentagon) and KECK II LRIS spectra (green triangle) with photoionization, shocks and the composite shock + precursor models shown. The green triangle corresponds to the emission line ratios from the KECK II data from Vernet et al. (2001). See Fig. 7 for more details.

can also estimate its radius using the velocity gradient of the H α absorption feature. Assuming the shell is spherical and using the velocity gradient of 30 km s^{-1} measured between $r = 0$ and $r = 14 \text{ kpc}$ (see Figs 12a and c), we obtain $R \sim 38 \text{ kpc}$, which is much smaller than the value derived by Gullberg et al. (2016) using the

maximum observed spatial offset of the absorber (60 kpc), perhaps indicating that the shell is not spherically symmetric.

Assuming the absorber is a spherical shell with uniform column density, and assuming its covering factor is 1 based on the fact that the absorption feature is black at its centre, we calculate the mass

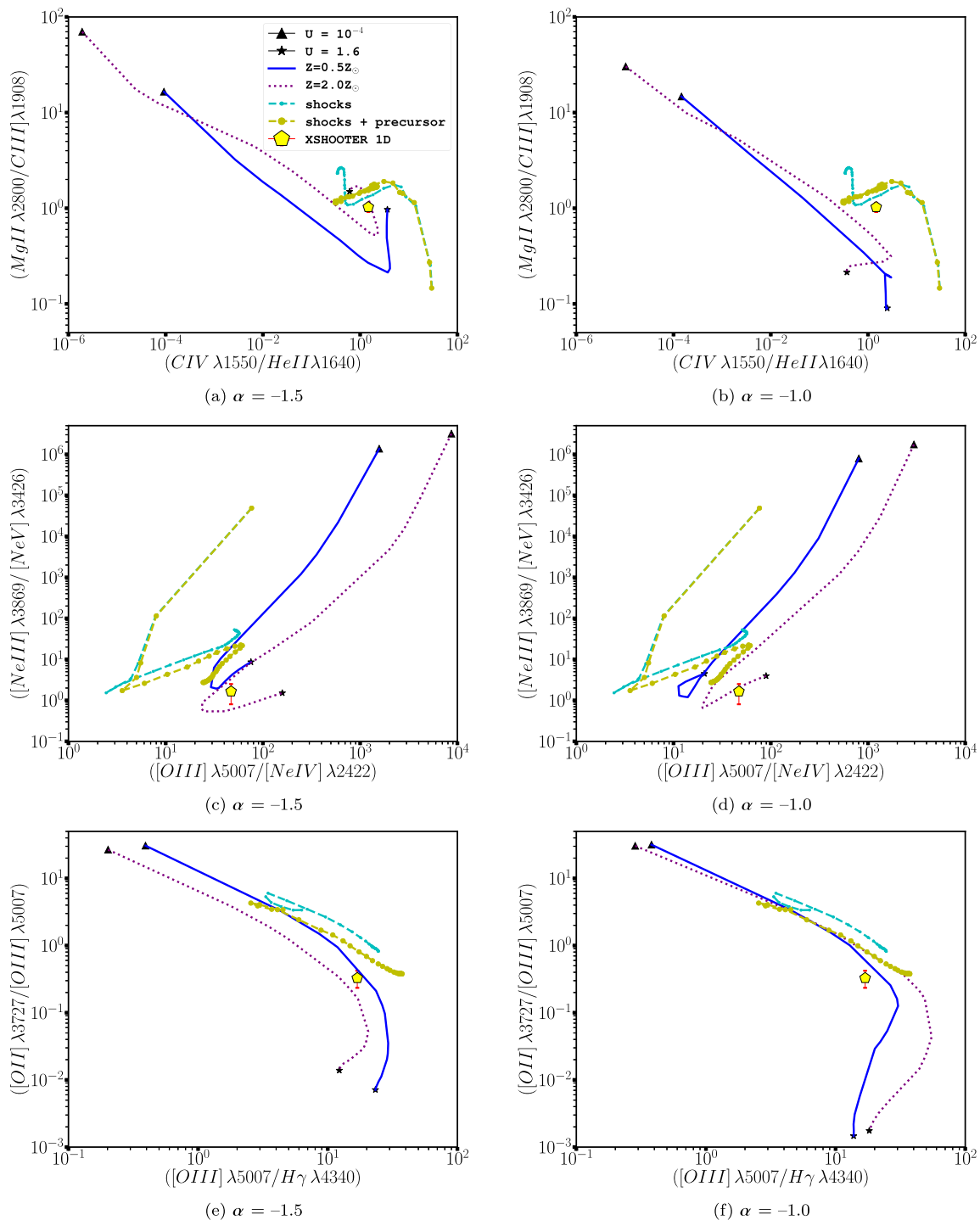


Figure 9. Comparison of the observed emission line ratios using integrated spectra from the X-SHOOTER long-slit (yellow pentagon) with photoionization, shocks and the composite shock + precursor models. See Fig. 7 for more details.

of the absorber using the expression

$$M_{\text{H}} \gtrsim 3.6 \times 10^9 (R/60 \text{ kpc})^2 (N_{\text{H}}/10^{19} \text{ cm}^{-2}) M_{\odot}, \quad (2)$$

where R is the radius of the absorption system in kpc and N_{H} is the H column density in cm^{-2} . Assuming $R \gtrsim 60 \text{ kpc}$ and $N_{\text{H}} \gtrsim 5 \times 10^{17} \text{ cm}^{-2}$, we obtain the hard lower limit $\log(M_{\text{H}}/M_{\odot}) \gtrsim 8.3$.

Clearly, because this is a lower limit, the mass of the shell could be even more massive than $\log(M_{\text{H}}/M_{\odot}) \gtrsim 8.3$. Indeed, if we were instead to use the value from our high column density fit

($\log N(\text{H I}/\text{cm}^{-2}) = 19.63$) and assume that the absorber is entirely neutral, we would then obtain $\log(M_{\text{H}}/M_{\odot}) \gtrsim 10.2$. If one were to assume the gas is partially ionized would lead to an even higher limit.

5.4 On the evolutionary status of MRC 0943–242

With a stellar mass of $\sim 10^{11.2} M_{\odot}$ (Seymour et al. 2007), MRC 0943–242 is remarkably massive for its redshift of 2.92. Significant

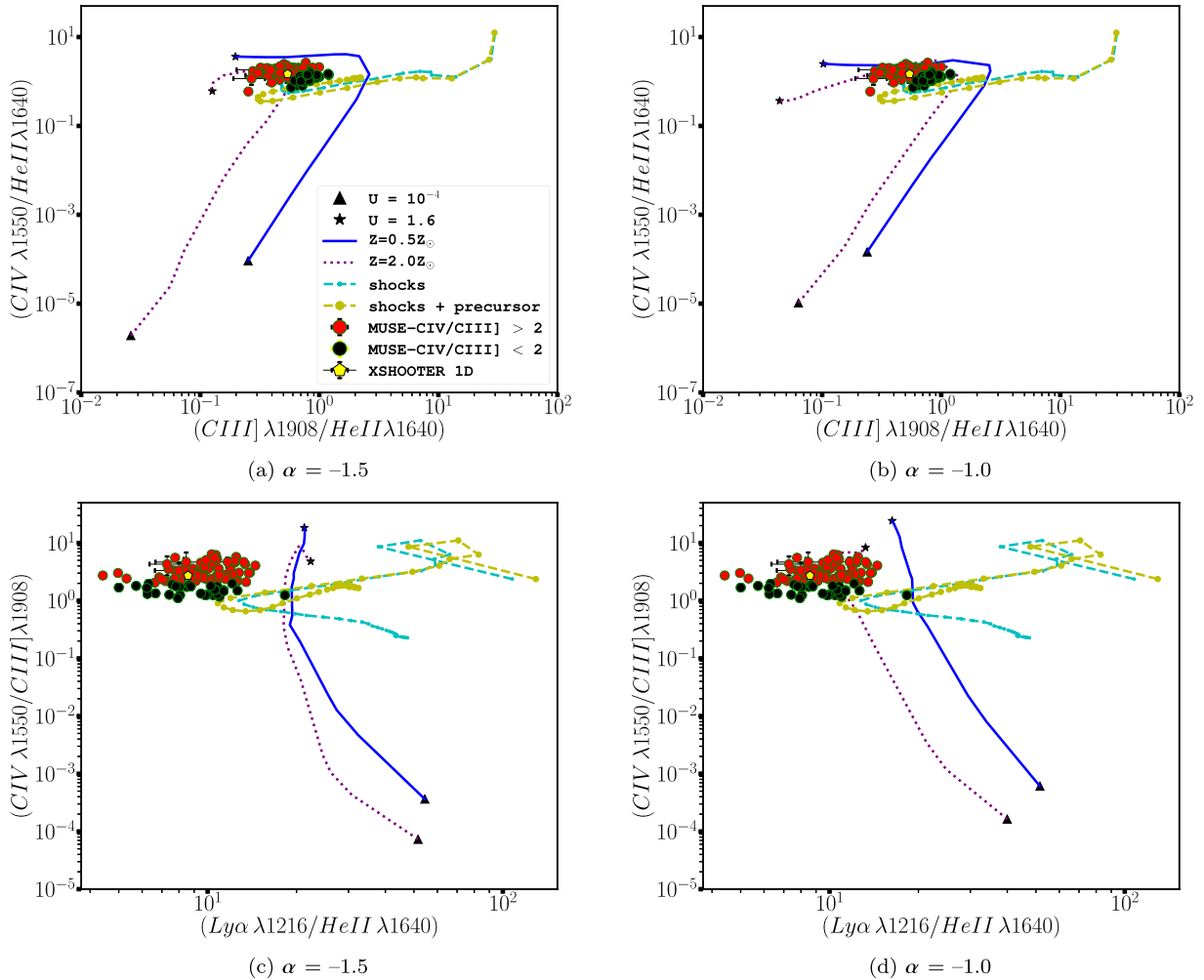


Figure 10. Comparison of the observed spatial variation of the MUSE UV emission line ratios with photoionization models ($0.5Z_{\odot}$ sequence is represented by the solid blue line and the $2.0Z_{\odot}$ sequence by the purple dotted line), pure shock models (blue solid circles connected by a dashed line) and the composite shock + precursor models (large yellow solid circles connected by a dashed line). In the case of the photoionization models, we use ionizing continuum power-law index $\alpha = -1.5$ (left-hand side) or $\alpha = -1.0$ (right-hand side). The red circles represent the regions in which $C\text{IV}/C\text{III}] > 2$, while the black circles represent that regions with $C\text{IV}/C\text{III}] < 2$ that lie close to the positions of the radio hotspots. The yellow pentagon represents the integrated spectrum extracted from the X-SHOOTER data. At the end of each sequence, a solid black triangle corresponds to the initial value of the ionization parameter ($U = 10^{-4}$) and a solid black star that corresponds to the maximum value of the ionization parameter ($U = 1.6$). The pure shock and the composite shock + precursor models are from Allen et al. (2008). Both shock model sequences are characterized by hydrogen density 100 cm^{-3} , magnetic field $100\text{ }\mu\text{G}$ and velocity covering the range $v_s = 100$ up to 1000 km s^{-1} .

SF activity is present in the host galaxy ($\sim 200\text{ M}_{\odot}\text{ yr}^{-1}$) and in companion galaxies ($\sim 1400\text{ M}_{\odot}\text{ yr}^{-1}$; Gullberg et al. 2016), and the powerful active nucleus appears to be subjecting its associated extended gas reservoir to substantial radio- and quasar-mode feedback. In the long run, this feedback activity may quench the modest SF activity found in the host galaxy, but our kinematic results suggest that processes related to the radio-mode feedback are drawing gas deeper into the potential well of the galaxy, and we speculate this could give rise to a short-lived enhancement in SF and the fuelling of the AGN. Indeed, this would be consistent with the reported anticorrelation between the luminosity of young stellar populations in HzRGs and the age of their radio sources (Humphrey et al. 2006).

The very high metallicity of the ionized gas within the radio galaxy demonstrates the presence of an already highly enriched gas, compatible with the scenario that this system could evolve into a passive spheroidal system characterized by supersolar metallicity

(e.g. Lonoce et al. 2015 and references therein; see also Vernet et al. 2001).

Interestingly, the high gas metallicity appears inconsistent with the scenario of smooth accretion of pristine gas, because in that scenario the gas metallicity should be low (e.g. Dekel et al. 2009). Although there is evidence for filamentary gas accretion into MRC 0943–242, the filamentary material appears to be dusty and metal enriched (Gullberg et al. 2016) and thus is likely to have been stripped from companion galaxies, rather than being low metallicity gas from the cosmic web. In fact, there appears to be no convincing evidence for smooth accretion of pristine gas in MRC 0943–242, although we cannot rule out the presence of faint, filamentary accretion structures of the kind detected near the $z = 3.1$ radio galaxy MRC 0316–257 (Vernet et al. 2017).

In summary, we suggest that we are witnessing MRC 0943–242 after the bulk of gas accretion has taken place, and the galaxy is

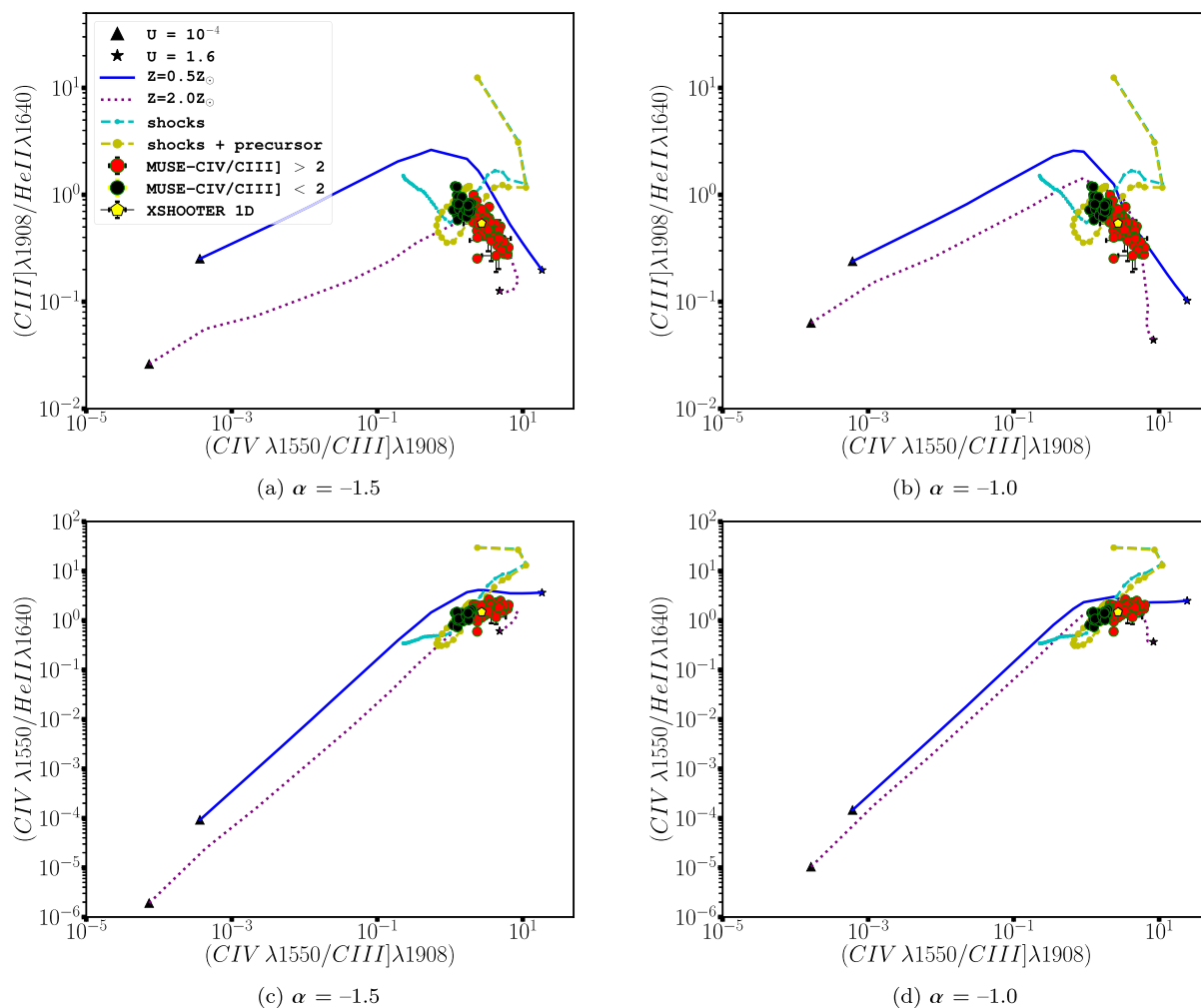


Figure 11. Comparison of the observed spatial variation of the MUSE UV emission line ratios with photoionization models ($0.5Z_{\odot}$ sequence is represented by the solid blue line and the $2.0Z_{\odot}$ sequence by the purple dotted line), pure shock models (blue solid circles connected by a dashed line) and the composite shock + precursor models (large yellow solid circles connected by a dashed line). In the case of the photoionization models, we use ionizing continuum power-law index $\alpha = -1.5$ (left-hand side) or $\alpha = -1.0$ (right-hand side). See Fig. 10 for more details.

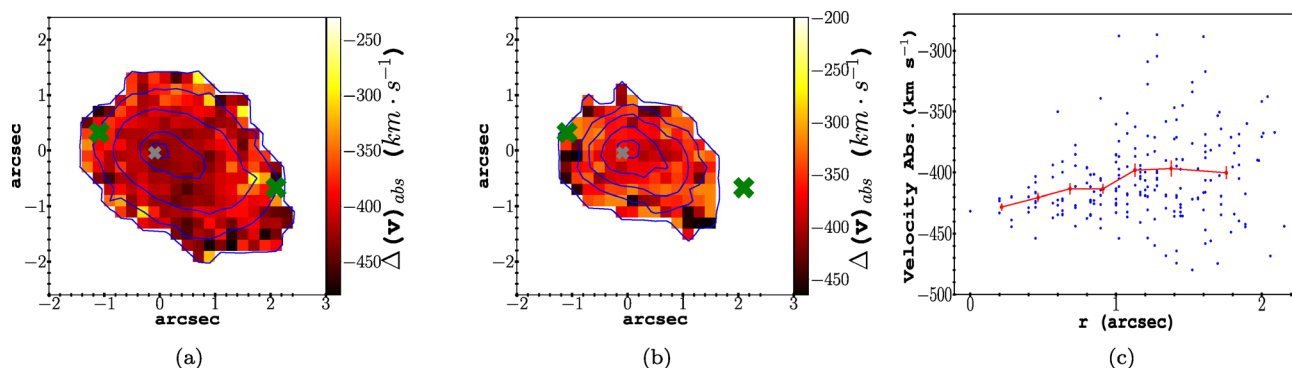


Figure 12. (a) Velocity offset map of the main absorber in the $\text{Ly}\alpha$ profile extracted from the MUSE IFU data. The velocity offset was measured relative to the He II emission line at the centre of the radio galaxy. The map also shows the contour levels of the emission-line intensity recovered by the fitting procedure. Contour levels: $(0.3, 1.3, 3.8, 12.5, 16.8) \times 10^{-16} \text{ erg cm}^{-2} \text{ s}^{-1} \text{ arcsec}^{-2}$. (b) Velocity offset map for the absorption trough in C IV profile extracted from MUSE IFU. The velocity offset was measured relative to the He II emission line at the centre of the radio galaxy. The map also shows the contour levels of the emission-line intensity recovered by the fitting procedure. Contour levels: $(0.5, 1.0, 2.0, 3.5, 4.3) \times 10^{-16} \text{ erg cm}^{-2} \text{ s}^{-1} \text{ arcsec}^{-2}$. The green 'X' represent the positions of the radio hotspots and the grey 'x' the position of the AGN. (c) The diagram shows the velocity offset of the main $\text{Ly}\alpha$ absorption as a function of the projected distance from the centre of the galaxy. The black points are the individual pixels, and the red points are bins in distance, with their 1σ error bars. Evaluating the strengths of correlation between the velocity offset of the main absorber and the projected distance using Spearman's rho and t-distribution, we find $\rho = 0.24$ with a p-value = 0.0003 (for unbinned data) and $\rho = 0.86$ with a p-value = 0.014 (for binned data).

now moving towards transformation into a spheroidal galaxy where the AGN feedback will probably, ultimately quench the SF.

6 CONCLUSIONS

Making use of observations from MUSE, X-SHOOTER and other instruments, we have studied the kinematic, chemical and excitation properties of the giant Ly α emitting halo and the giant H I absorber associated with the $z = 2.92$ radio galaxy MRC 0943–242. The main conclusions of this study are summarized as follows.

(i) We find clear evidence for jet–gas interactions affecting the kinematic properties of the Ly α nebula of MRC 0943–242. The MUSE data cube reveals a region of kinematically turbulent gas with relatively high FWHM extending from the nucleus out to the positions of the radio hotspots, where we see the most extreme kinematic properties, beyond which the gas has rather more quiescent kinematics in agreement with the long-slit study of Villar-Martín et al. (2003). The gas most closely associated with the radio hotspots shows a blueshift relative to other regions, consistent with jet-induced outflows. However, at smaller radii the emission-line gas shows a relative redshift, even compared to the kinematically quiescent gas, which we suggest might signal the presence of a feedback-driven *inflow* due to gas being pulled inwards as part of the entrainment process, and/or a backflow of material from the radio hotspots.

(ii) We have computed a grid of photoionization models, to which we have added shock ionization models from the literature (Allen et al. 2008), and have searched for the model that best reproduces the complete ensemble of emission-line relative fluxes measured from our X-SHOOTER spectrum. We find that a photoionization model with a moderate ionization parameter ($U = 0.018$), a relatively hard ionizing SED ($\alpha = -1.0$) and a high gas metallicity ($Z/Z_{\odot} = 2.1$) provides the best overall fit. However, we note that the [O III] $\lambda 4363$ / [O III] $\lambda 5007$ flux ratio is not well reproduced by this model, suggesting the presence of some shock-heating in the extended gas. In addition, the apparent inability to simultaneously reproduce lines of all ionization states suggests the presence of clouds with a substantial range in U , a result that is validated by our analysis of the 2D ionization properties.

(iii) We find a substantial range in ionization level across the object, with a clear spatial correlation between the radio hotspots and UV emission line ratios indicative of relatively low ionization that we suggest may be due to shock-heating and/or the compression of gas by the radio source. We also find evidence for a lower Ly α escape fraction in regions unaffected by radio-mode feedback, and speculate scenarios that may explain this result: (1) reduction of dust in the kinematically perturbed regions due to jet-driven shocks (e.g. Villar-Martín et al. 2001); (2) greater velocity overlap between emitting and absorbing gas phases in the kinematically quiescent regions (e.g. Tenorio-Tagle et al. 1999); and (3) the presence of an optically thick shell of gas encasing the expanding radio cocoon (e.g. Binette et al. 2006).

(iv) Our Ly α /He II flux-ratio map reveals a large range of values across the nebula, with most spaxels having values lower than the ionization in our grid. We attribute this to an inhomogeneity in the impact of transfer effects such as quenching by dust and/or the scattering of Ly α photons into different sight-lines.

(v) We identify and explore a strong degeneracy between column density and Doppler width of the strong, blueshifted H I Ly α absorber. We have been able to obtain a reasonable fit to the absorption feature across the range $\log N(\text{H I}/\text{cm}^{-2}) = 15.20$ and 19.63,

with the best fitting occurring near the extreme ends of this range. Independently of our fits to Ly α , we use N_{CIV} to obtain a lower limit to the total H column density of $N_{\text{H}} \gtrsim 5 \times 10^{17} \text{ cm}^{-2}$. Given the lower limit of the spatial extent of the H I obtained with the absorber velocity map, we assume a spherical shell of gas with radius $\gtrsim 60$ kpc obtained by Gullberg et al. (2016). Assuming $N_{\text{H}} \gtrsim 5 \times 10^{17} \text{ cm}^{-2}$, the shell would have $\log (M_{\text{H}}/M_{\odot}) \gtrsim 8.3$.

ACKNOWLEDGEMENTS

MS acknowledges support from the National Council of Research and Development (CNPq) under the process of number 248617/2013-3. AH acknowledges FCT support through fellowship SFRH/BPD/107919/2015. PL acknowledges support by the FCT through the grant SFRH/BPD/72308/2010. MVM acknowledges support from the Spanish Ministerio de Economía y Competitividad through the grant AYA2015-64346-C2-2-P. MS, AH, PL and SM acknowledge project FCOMP-01-0124-FEDER-029170 (Reference FCT PTDC/FIS-AST/3214/2012), funded by the FEDER programme. We also thank Bitten Gullberg and Carlos De Breuck for making available the reduced MUSE data cube of MRC 0943–242.

REFERENCES

- Allen M. G., Groves B. A., Dopita M. A., Sutherland R. S., Kewley L. J., 2008, *ApJS*, 178, 20
- Asplund M., Grevesse N., Jacques Sauval A., 2006, *Nucl. Phys. A*, 777, 1
- Bacon R. et al., 2010, *Proc. SPIE Vol. 7735, Ground-based and Airborne Instrumentation for Astronomy III*. SPIE, Bellingham, p. 773508
- Bacon R. et al., 2014, *The Messenger*, 157, 13
- Binette L., Dopita M. A., Tuohy I. R., 1985, *ApJ*, 297, 476
- Binette L., Kurk J. D., Villar-Martín M., Röttgering H. J. A., 2000, *A&A*, 356, 23
- Binette L., Wilman R. J., Villar-Martín M., Fosbury R. A. E., Jarvis M. J., Röttgering H. J. A., 2006, *A&A*, 459, 31
- Binette L., Benítez E., Villar-Martín M., de Diego J.-A., Haro-Corzo S., Humphrey A., 2007, in Guzmán R., ed., *Rev. Mex. Astron. Astrofis. Conf. Ser. Vol. 29, First Light Science with the GTC*. p. 129.
- Borisova E. et al., 2016, *ApJ*, 831, 39
- Cai Z. et al., 2017, *ApJ*, 837, 71
- Cantalupo S., Arrigoni-Battaia F., Prochaska J. X., Hennawi J. F., Madau P., 2014, *Nature*, 506, 63
- Cardelli J. A., Clayton G. C., Mathis J. S., 1989, *ApJ*, 345, 245
- Carilli C. L., Röttgering H. J. A., van Ojik R., Miley G. K., van Breugel W. J. M., 1997, *ApJS*, 109, 1
- De Breuck C., Röttgering H., Miley G., van Breugel W., Best P., 2000, *A&A*, 362, 519
- Dekel A. et al., 2009, *Nature*, 457, 451
- di Serego Alighieri S., 1988, in Arp H. C., ed., *New Ideas in Astronomy*. p. 111
- Dijkstra M., Loeb A., 2009, *MNRAS*, 400, 1109
- Dijkstra M., Haimes Z., Spaans M., 2006, *ApJ*, 649, 14
- Emonts B. H. C., Morganti R., Tadhunter C. N., Oosterloo T. A., Holt J., van der Hulst J. M., 2005, *MNRAS*, 362, 931
- Emonts B. H. C. et al., 2011, *MNRAS*, 415, 655
- Fardal M. A., Katz N., Gardner J. P., Hernquist L., Weinberg D. H., Davé R., 2001, *ApJ*, 562, 605
- Faucher-Giguère C.-A., Kereš D., Dijkstra M., Hernquist L., Zaldarriaga M., 2010, *ApJ*, 725, 633
- Ferruit P., Binette L., Sutherland R. S., Pecontal E., 1997, *A&A*, 322, 73
- Fitzpatrick E. L., 1999, *PASP*, 111, 63
- Fosbury R. A. E. et al., 1982, *MNRAS*, 201, 991
- Francis P. J. et al., 2001, *ApJ*, 554, 1001
- Geach J. E. et al., 2009, *ApJ*, 700, 1

- Gould A., Weinberg D. H., 1996, *ApJ*, 468, 462
 Gullberg B. et al., 2016, *A&A*, 586, A124
 Haiman Z., Spaans M., Quataert E., 2000, *ApJ*, 537, L5
 Henry R. B. C., Edmunds M. G., Köppen J., 2000, *ApJ*, 541, 660
 Hinshaw G. et al., 2013, *ApJS*, 208, 19
 Humphrey A., Villar-Martín M., Fosbury R., Vernet J., di Serego Alighieri S., 2006, *MNRAS*, 369, 1103
 Humphrey A., Villar-Martín M., Fosbury R., Binette L., Vernet J., De Breuck C., di Serego Alighieri S., 2007, *MNRAS*, 375, 705
 Humphrey A., Villar-Martín M., Vernet J., Fosbury R., di Serego Alighieri S., Binette L., 2008a, *MNRAS*, 383, 11
 Humphrey A. et al., 2008b, *MNRAS*, 390, 1505
 Humphrey A. et al., 2011, *MNRAS*, 418, 74
 Humphrey A., Binette L., Villar-Martín M., Aretxaga I., Papaderos P., 2013a, *MNRAS*, 428, 563
 Humphrey A., Vernet J., Villar-Martín M., di Serego Alighieri S., Fosbury R. A. E., Cimatti A., 2013b, *ApJ*, 768, L3
 Jarvis M. J., Wilman R. J., Röttgering H. J. A., Binette L., 2003, *MNRAS*, 338, 263
 Kollmeier J. A., Zheng Z., Davé R., Gould A., Katz N., Miralda-Escudé J., Weinberg D. H., 2010, *ApJ*, 708, 1048
 Large M. I., Mills B. Y., Little A. G., Crawford D. F., Sutton J. M., 1981, *MNRAS*, 194, 693
 Lonoce I. et al., 2015, *MNRAS*, 454, 3912
 McCarthy P. J., 1993, *ARA&A*, 31, 639
 McCarthy P. J., Spinrad H., Dickinson M., van Breugel W., Liebert J., Djorgovski S., Eisenhardt P., 1990, *ApJ*, 365, 487
 McCarthy P. J., Spinrad H., van Breugel W., 1995, *ApJS*, 99, 27
 Newville M., Stensitzki T., Allen D. B., Ingargiola A., 2014, *LMFIT: Non-Linear Least-Square Minimization and Curve-Fitting for Python*
 Pentericci L., Röttgering H. J. A., Miley G. K., Spinrad H., McCarthy P. J., van Breugel W. J. M., Macchetto F., 1998, *ApJ*, 504, 139
 Pentericci L., Röttgering H. J. A., Miley G. K., McCarthy P., Spinrad H., van Breugel W. J. M., Macchetto F., 1999, *A&A*, 341, 329
 Pentericci L., McCarthy P. J., Röttgering H. J. A., Miley G. K., van Breugel W. J. M., Fosbury R., 2001, *ApJS*, 135, 63
 Reuland M. et al., 2003, *ApJ*, 592, 755
 Rosdahl J., Blaizot J., 2012, *MNRAS*, 423, 344
 Röttgering H. J. A., Lacy M., Miley G. K., Chambers K. C., Saunders R., 1994, *A&AS*, 108
 Röttgering H. J. A., Hunstead R. W., Miley G. K., van Ojik R., Wieringa M. H., 1995, *MNRAS*, 277, 389
 Röttgering H. J. A., van Ojik R., Miley G. K., Chambers K. C., van Breugel W. J. M., de Koff S., 1997, *A&A*, 326, 505
 Sánchez S. F., Humphrey A., 2009, *A&A*, 495, 471
 Seymour N. et al., 2007, *ApJS*, 171, 353
 Steidel C. C., Adelberger K. L., Shapley A. E., Pettini M., Dickinson M., Giavalisco M., 2000, *ApJ*, 532, 170
 Swinbank A. M. et al., 2015, *MNRAS*, 449, 1298
 Tadhunter C. N., Robinson A., Morganti R., 1989, in Meurs E. J. A., Fosbury R. A. E., eds, *ESO Conf. Proc. Vol. 32*, p. 293
 Tenorio-Tagle G., Silich S. A., Kunth D., Terlevich E., Terlevich R., 1999, *MNRAS*, 309, 332
 van Breugel W. J. M., Stanford S. A., Spinrad H., Stern D., Graham J. R., 1998, *ApJ*, 502, 614
 van Ojik R., Röttgering H. J. A., Carilli C. L., Miley G. K., Bremer M. N., Macchetto F., 1996, *A&A*, 313, 25
 van Ojik R., Röttgering H. J. A., Miley G. K., Hunstead R. W., 1997, *A&A*, 317, 358
 Venemans B. P. et al., 2007, *A&A*, 461, 823
 Vernet J., Fosbury R. A. E., Villar-Martín M., Cohen M. H., Cimatti A., di Serego Alighieri S., Goodrich R. W., 2001, *A&A*, 366, 7
 Vernet J. et al., 2011, *A&A*, 536, A105
 Vernet J. et al., 2017, *A&A*, 602, L6
 Villar-Martín M., Fosbury R. A. E., Binette L., Tadhunter C. N., Rocca-Volmerange B., 1999, *A&A*, 351, 47
 Villar-Martín M., De Young D., Alonso-Herrero A., Allen M., Binette L., 2001, *MNRAS*, 328, 848
 Villar-Martín M., Vernet J., di Serego Alighieri S., Fosbury R., Pentericci L., Cohen M., Goodrich R., Humphrey A., 2002, *MNRAS*, 336, 436
 Villar-Martín M., Vernet J., di Serego Alighieri S., Fosbury R., Humphrey A., Pentericci L., 2003, *MNRAS*, 346, 273
 Villar-Martín M., Sánchez S. F., Humphrey A., Dijkstra M., di Serego Alighieri S., De Breuck C., González Delgado R., 2007, *MNRAS*, 378, 416
 Wilman R. J., Jarvis M. J., Röttgering H. J. A., Binette L., 2004, *MNRAS*, 351, 1109
 Yang Y., Zabludoff A. I., Davé R., Eisenstein D. J., Pinto P. A., Katz N., Weinberg D. H., Barton E. J., 2006, *ApJ*, 640, 539
 Yang Y., Zabludoff A., Jahnke K., Davé R., 2014, *ApJ*, 793, 114

APPENDIX A: ADDITIONAL MATERIAL

Table A1. Measurements of the rest-frame UV and optical emission lines obtained with the fitting routine. $\text{Ly}\alpha_{15}$ and $\text{Ly}\alpha_{19}$ correspond to the lower ($\log N(\text{H}/\text{cm}^{-2}) \sim 15.20$) and higher ($\log N(\text{H}/\text{cm}^{-2}) \sim 19.63$) column density results, respectively.

Line	λ_{rest} Å	λ_{obs} Å	Line flux ($\times 10^{-16}$ erg cm^{-2} s^{-1})	FWHM (km s^{-1})	Δv (km s^{-1})
VLT UVES					
$\text{Ly}\alpha_{15}$	1215.7	4768.6 ± 0.1	26.95 ± 0.33	1516 ± 9	-161 ± 3
$\text{Ly}\alpha_{19}$	1215.7	4768.0 ± 0.1	31.03 ± 0.43	1439 ± 8	-199 ± 3
C IV	1548.2, 1550.8	$6076.1 \pm 0.2, 6086.3 \pm 0.1$	2.76 ± 0.08	1173 ± 29	-7 ± 11
AAT					
$\text{Ly}\alpha_{15}$	1215.7	4769.2 ± 0.2	14.36 ± 0.65	1529 ± 35	-11 ± 10
$\text{Ly}\alpha_{19}$	1215.7	4768.7 ± 0.2	16.46 ± 0.80	1486 ± 31	-45 ± 10
C IV	1548.2, 1550.8	$6071.3 \pm 0.4, 6081.5 \pm 0.1$	4.36 ± 0.34	1331 ± 66	-136 ± 18
He II	1640.4	6434.2 ± 0.6	1.41 ± 0.14	885 ± 69	0 ± 27
KECK II					
$\text{Ly}\alpha$	1215.7	4773.1 ± 0.2	19.76 ± 0.47	1695 ± 19	156 ± 9
N V	1238.8, 1242.8	$4864.1 \pm 0.5, 4879.7 \pm 0.5$	0.43 ± 0.05	1318 ± 125	162 ± 29
N IV]	1483.3, 1486.5	$5820.1 \pm 1.8, 5832.6 \pm 1.8$	0.11 ± 0.04	757 ± 193	-44 ± 93
C IV	1548.2, 1550.8	$6076.6 \pm 0.2, 6086.8 \pm 0.2$	2.75 ± 0.07	1183 ± 18	51 ± 12
He II	1640.4	6435.8 ± 0.2	1.94 ± 0.05	1098 ± 20	0 ± 8
O III]	1660.8, 1666.1	$6512.8 \pm 1.3, 6533.7 \pm 1.3$	0.30 ± 0.05	1320 ± 203	-215 ± 62
C III]	1906.7, 1908.7	$7480.9 \pm 0.3, 7488.9 \pm 0.3$	1.16 ± 0.04	1008 ± 32	-58 ± 11

Table A2. Best-fitting parameters for the Ly α absorption features, for different instruments. Column (1) gives the redshift for the Ly α emission Gaussian. Column (2) gives the redshift for each Ly α absorption. Column (3) gives the column density ($N(\text{H I})$). Column (4) gives the Doppler width b . Column (5) gives the velocity shift of the main absorber with respect to He II emission in the same spectrum.

Ly α emission redshift (z_{em})	Absorption redshift (z_{abs})	Column density (cm^{-2})	Doppler b parameter (km s^{-1})	Δv (km s^{-1})
VLT UVES				
2.922 13 \pm 0.000 04	2.906 74 \pm 0.000 06	(1.02 \pm 0.09) \times 10 ¹⁴	81 \pm 6	
	2.918 45 \pm 0.000 01	(4.29 \pm 0.11) \times 10 ¹⁹	54 \pm 1	
	2.926 18 \pm 0.000 04	(5.80 \pm 0.32) \times 10 ¹³	128 \pm 5	
	2.932 29 \pm 0.000 03	(3.33 \pm 0.20) \times 10 ¹³	50 \pm 3	
2.922 63 \pm 0.000 04	2.906 82 \pm 0.000 05	(8.65 \pm 0.89) \times 10 ¹³	56 \pm 5	
	2.918 40 \pm 0.000 01	(1.58 \pm 0.07) \times 10 ¹⁵	158 \pm 2	
	2.925 81 \pm 0.000 05	(4.99 \pm 0.38) \times 10 ¹³	138 \pm 8	
	2.932 32 \pm 0.000 03	(2.94 \pm 0.20) \times 10 ¹³	45 \pm 3	
AAT				
2.922 68 \pm 0.000 14	2.907 76 \pm 0.006 83	(9.43 \pm 2.83) \times 10 ¹³	82 \pm 30	
	2.919 47 \pm 0.000 03	(5.11 \pm 0.47) \times 10 ¹⁹	52 \pm 2	-290 ± 3
	2.926 96 \pm 0.000 13	(4.79 \pm 0.80) \times 10 ¹³	100 \pm 39	
	2.933 21 \pm 0.000 18	(2.85 \pm 0.81) \times 10 ¹³	50 \pm 26	
2.923 13 \pm 0.000 14	2.907 70 \pm 0.000 29	(6.72 \pm 2.66) \times 10 ¹³	65 \pm 33	
	2.919 44 \pm 0.000 05	(1.36 \pm 0.15) \times 10 ¹⁵	185 \pm 8	-293 ± 4
	2.926 60 \pm 0.000 14	(6.16 \pm 1.30) \times 10 ¹³	128 \pm 22	
	2.933 28 \pm 0.000 20	(2.81 \pm 0.88) \times 10 ¹³	56 \pm 3	

Note. The He II emission line was outside the spectral range covered by the red arm of VLT UVES and thus we do not give the velocity shift for this instrument.

Table A3. Best-fitting parameters for the C IV absorption features, for different instruments. Column (1) gives the redshift for the C IV emission. Column (2) gives the redshift for each C IV absorption. Column (3) gives the column density ($N(\text{C IV})$). Column (4) gives the Doppler width b . Column (5) gives the velocity shift of the main absorber with respect to He II emission in the same spectrum.

CIV emission redshift (z_{em})	Absorption redshift (z_{abs})	Column density (cm^{-2})	Doppler parameter (km s^{-1})	Δv (km s^{-1})
VLT UVES				
2.924 59 \pm 0.000 15	2.918 99 \pm 0.000 01	(3.04 \pm 0.24) \times 10 ¹⁴	67 \pm 5	
AAT				
2.921 49 \pm 0.000 08	2.919 50 \pm 0.000 03	(3.89 \pm 0.54) \times 10 ¹⁴	140 \pm 15	-288 ± 8

Note. The He II emission line was outside the spectral range covered by the red arm of VLT UVES and thus we do not give the velocity shift for this instrument.

;

;

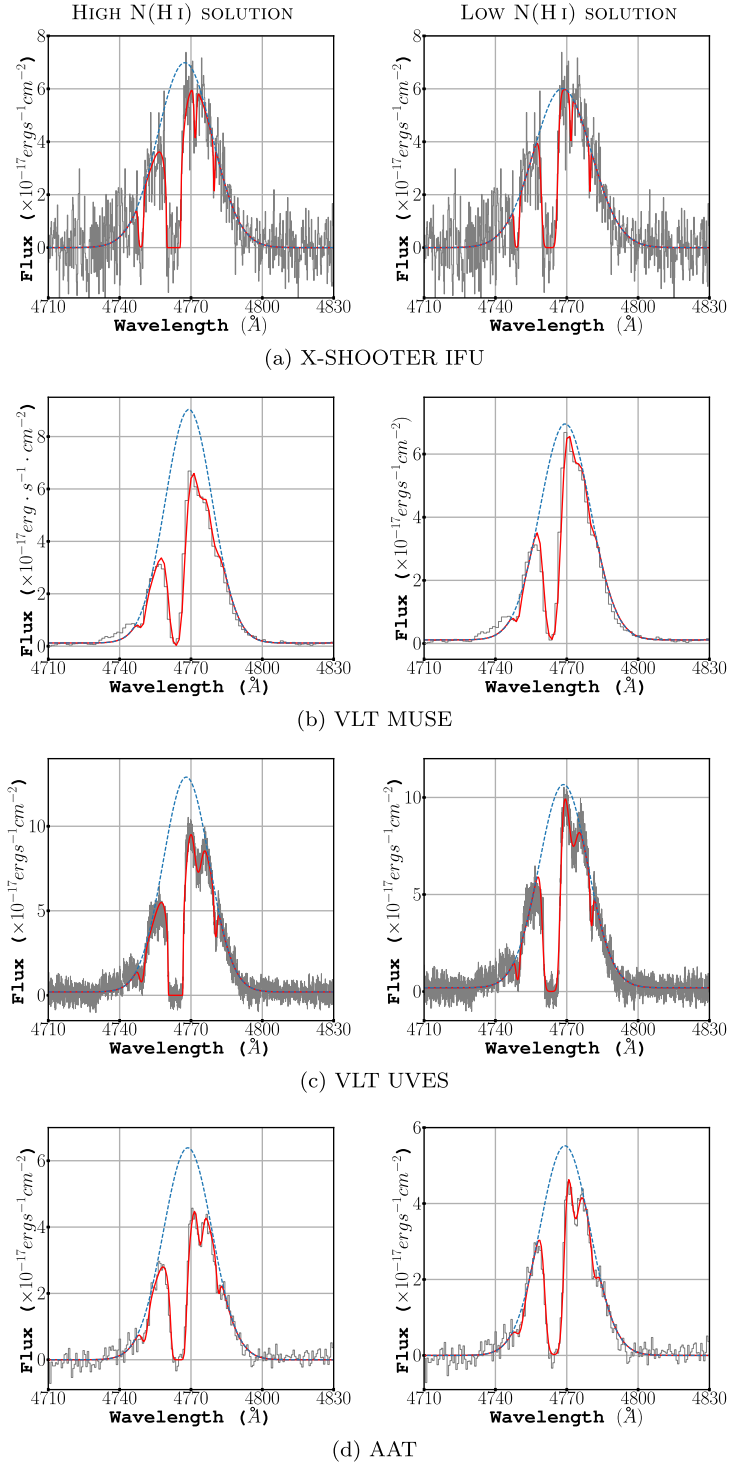


Figure A1. Ly α profile of MRC 0943–242 extracted from different instruments, with the Gaussian emission component (dashed blue line) plus absorption model overlaid (red line). The left- and right-hand columns show the high and low column density best fitting, respectively. The Ly α profile from the MUSE IFU was extracted using a circular aperture of 0.8 arcsec.

;

;

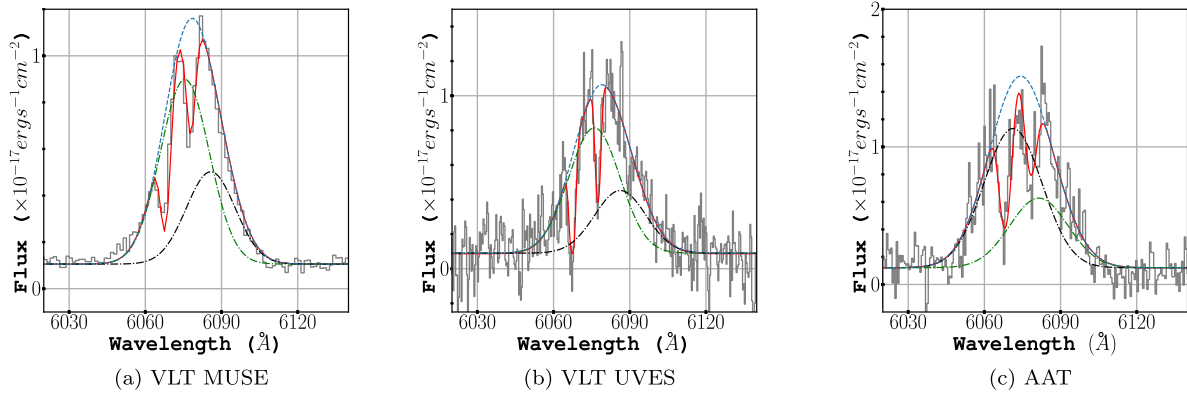


Figure A2. The C IV profile of MRC 0943–242, with the Gaussian emission component (dashed blue line) and emission plus absorption model overlaid (red line). The two individual doublet components are also shown.

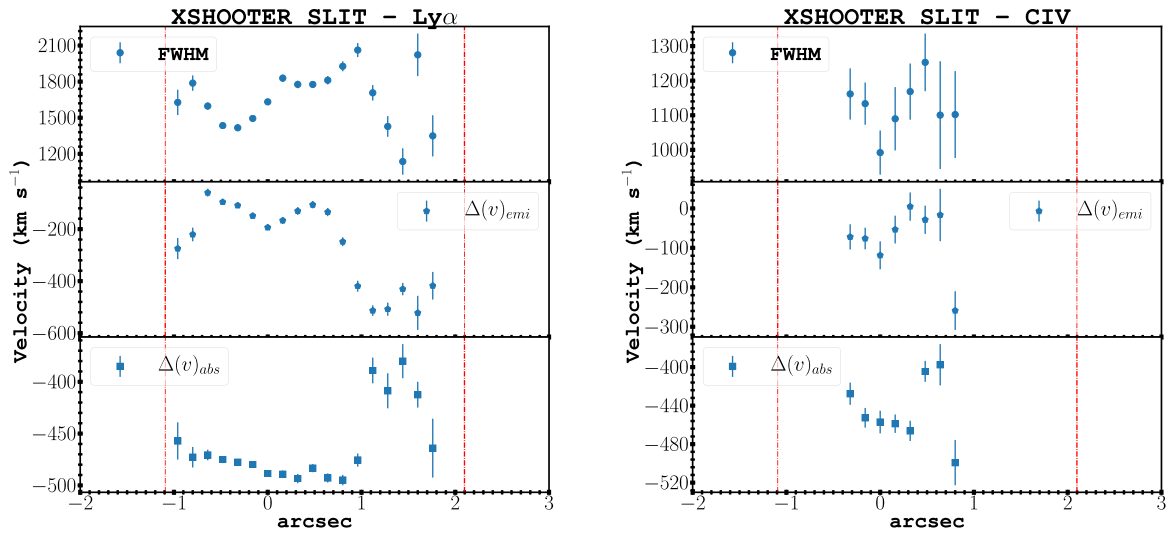


Figure A3. Kinematic properties of the MRC 0943–242 radio galaxy extracted from the X-SHOOTER SLIT data. We present the velocity dispersion for the emission lines and velocity offset for the emission and absorption lines as a function of the position along the slit in arcseconds. The red dashed–dotted lines represent the positions of the radio hotspots.

;

;

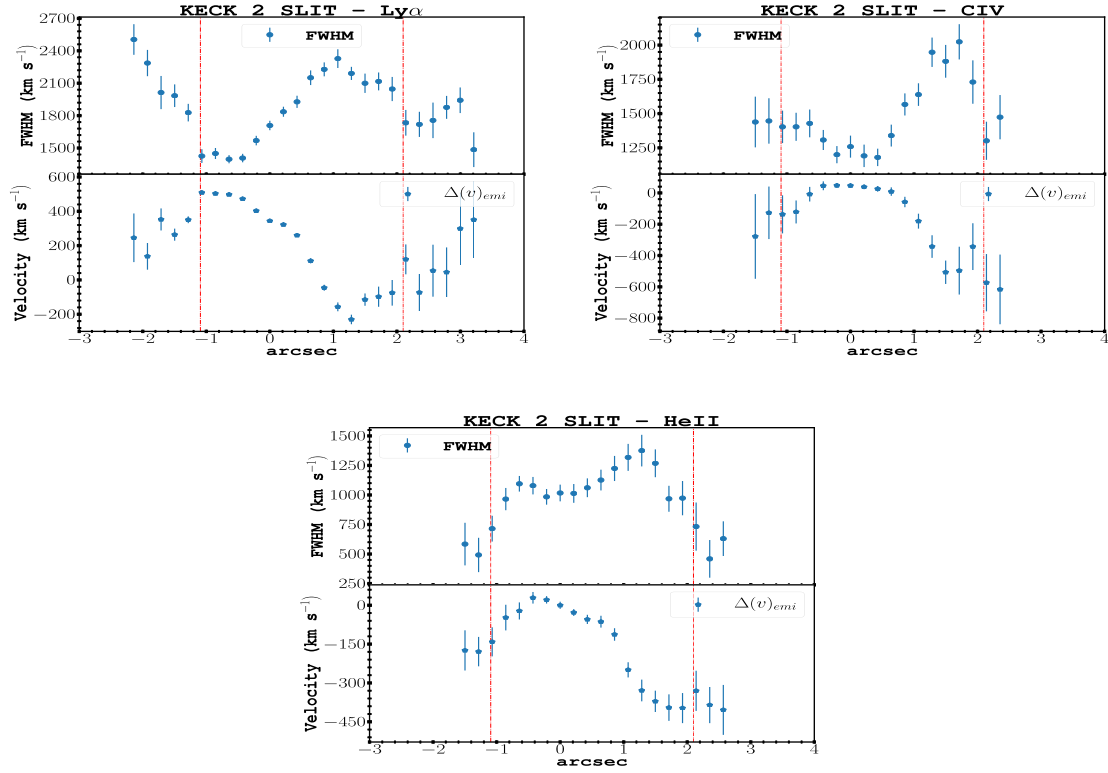


Figure A4. Kinematic properties of the MRC 0943–242 radio galaxy extracted from KECK II long slit. The red dashed–dotted lines represent the positions of the radio hotspots.

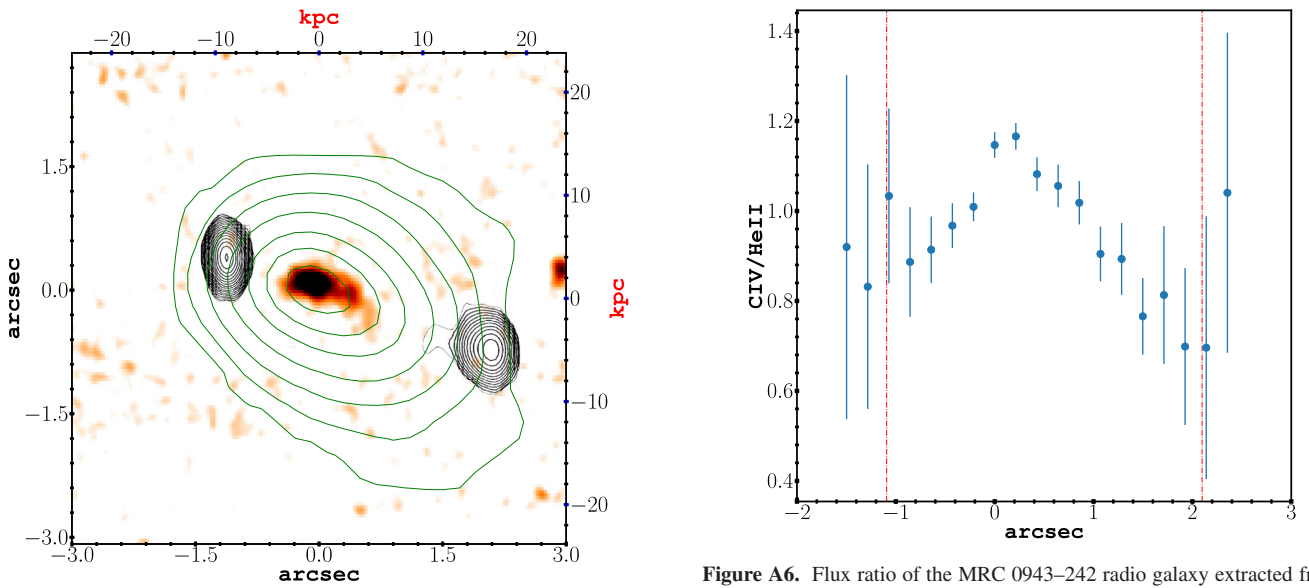


Figure A5. An *HST* NICMOS continuum image of MRC 0943–242 at $z = 2.92$ with VLA radio contours (black) and Ly α contours (green; see Fig. 4a) superimposed.

Figure A6. Flux ratio of the MRC 0943–242 radio galaxy extracted from the KECK II slit data. The red dashed–dotted lines represent the positions of the radio hotspots.

;

;

Table A4. Comparison of model line ratios with observed line ratios. Column (1): emission line ratios; column (2): observed X-SHOOTER line fluxes normalized by He II $\lambda 1640$ using a larger (2.1 arcsec) aperture; column (3): parameters and relative line fluxes produced by our best-fitting MAPPINGS model; column (4): our best-fitting model using $\alpha = -1.5$ instead of $\alpha = -1.0$; column (5): parameters and relative line fluxes produced by our best-fitting shock models; and column (6): shock + precursor models extracted from Allen et al. (2008).

Line ratios (1)	Obs. flux (2)	Model 01 (3)	Model 02 (4)	Model 03 (5)	Model 04 (6)
		$U = 0.019$ $\alpha = -1.0$ $Z/Z_{\odot} = 1.8$ $\chi^2_v = 3.11$	$U = 0.035$ $\alpha = -1.5$ $Z/Z_{\odot} = 1.1$ $\chi^2_v = 6.44$	shocks $v = 200 \text{ km s}^{-1}$ $Z/Z_{\odot} = 1.0$ $\chi^2_v = 7.41$	shock + prec. $v = 750 \text{ km s}^{-1}$ $Z/Z_{\odot} = 1.0$ $\chi^2_v = 8.24$
Ly α^a /He II	7.88 ± 0.26	10.53	16.47	58.65	29.06
(O VI+C II)/He II	0.87 ± 0.10	0.48	0.31	3.70	4.51
N V/He II	0.70 ± 0.03	0.47	0.23	3.78	0.33
C IV/He II	1.21 ± 0.11	2.47	2.25	8.60	2.22
C III]/He II	0.55 ± 0.02	1.34	1.10	1.62	1.21
C II]/He II	0.24 ± 0.01	0.16	0.08	1.14	0.64
[Ne IV]/He II	0.21 ± 0.02	0.45	0.31	1.22	0.28
Mg II/He II	0.42 ± 0.03	0.48	0.45	2.16	2.01
[Ne V]/He II	0.66 ± 0.04	0.63	0.45	0.53	0.34
[O II]/He II	2.84 ± 0.08	0.84	0.44	3.25	3.02
[Ne III]/He II	0.99 ± 0.04	0.71	0.85	0.81	1.20
H γ /He II	0.38 ± 0.04	0.17	0.31	0.83	0.22
[O III]4363/He II	0.27 ± 0.02	0.13	0.10	0.23	0.13
[O III]5007/He II	7.97 ± 0.21	8.94	8.65	2.75	8.02

Note:^aLy α was not used in the fitting.

This paper has been typeset from a $\text{\TeX}/\text{\LaTeX}$ file prepared by the author.